ORIGINAL PAPER

Experimental Study on the Time-Dependent Gas Permeability of Fractures in Shales

Ning Zhu[1] · Pengju Cheng[2] · Qingchun Yu[1]

Abstract

The gas permeabilities of shale fractures provide a critical basis for deeply understanding the subsurface fluid flow processes in many underground engineering activities in shales. However, the time-dependent behavior of shale permeability under formation stress has been rarely reported. In this study, two artificially fractured shale cores were used to experimentally investigate the time dependence of the fracture gas permeability and underlying mechanisms. Daily measurements of permeabilities were conducted at various gas pressures under multilevel confining stresses, where the confining stress was incrementally changed from 10 to 25 MPa and then reverted to 10 MPa. Numerical calculations were performed to determine the fracture apertures. The experimental results reveal a notable decline in gas permeability and aperture over time under each confining stress during the loading phase that proceeds from a decelerating decline stage to a steady decline stage. The gas permeability can be overestimated by at least a factor of 2 due to fracture creep. The magnitude of time-dependent permeability reduction is related to the fracture geometry, contact area, spatial distribution of apertures, and fracture stiffness. The observed significant permeability loss and limited time-dependent permeability recovery during the unloading stage indicate an irrecoverable process of creep-induced permeability reduction. The gas pressure-dependent permeability suggests notable gas slippage in fractures, which is influenced by creep and exhibits a power function decay with time. Considering the coupling effect of stress creep and gas slippage, a time-dependent gas permeability model is developed and validated using experimental data. This model is helpful to effectively predict the variation trend of fracture permeability during the implementation of underground engineering.

Highlights

- Time-dependent variations in gas permeability of shale fractures were measured and analyzed under multilevel confining stresses.
- Gas slippage phenomenon was observed in the fracture and decayed as a power function with time.
- A gas permeability model of fracture that considers the coupled effects of creep compaction and gas slippage was proposed and validated against experimental data.

✉ Qingchun Yu
yuqch@cugb.edu.cn

1 Beijing Key Laboratory of Water Resources and Environmental Engineering, School of Water Resource and Environment, China University of Geosciences (Beijing), Beijing 100083, China

2 China National Engineering Research Center for Utilization of Industrial Minerals, Zhengzhou Institute of Multipurpose Utilization of Mineral Resources, CAGS, Zhengzhou 450006, China

1 Introduction

Shales are generally characterized by low porosity, extremely low permeability, and excellent sealing ability, which make them ideal caprocks for gas geological disposal. Due to their abundant hydrocarbon content, shales also serve as unconventional reservoir rocks (Bachu 2000; Cheng and Yu 2019). Many underground engineering practices in shales, such as hydraulic fracturing or massive-scale gas injection in underground storage projects, induce numerous microfractures or reactivate preexisting microfractures. Such fractures provide

the main transport pathways for fluids in shale (Watanabe et al. 2008). The fluid flow process in fractures is critical in many engineering activities, including the production of oil and gas reservoirs (Cho et al. 2013; Deng et al. 2014; Zhang et al. 2021), effective recovery of hydrocarbons or geothermal fluids (Bandara et al. 2021; Cheng et al. 2021), evaluation of caprock sealing performance in CO_2 sequestration (Busch et al. 2008; Cheng and Yu 2022), and long-term storage of radioactive waste (Berkowitz 2002; Chen et al. 2022). Shales containing clay and soft materials exhibit time-dependent deformation characteristics under formation stress (i.e., creep), which results in variations in the aperture structure and long-term transport capacity of fractures (Liang et al. 2020; Matsuki et al. 2001). The altered aperture structures (the aperture magnitude and distribution, the contact area, etc.) and the resulting transport properties of fractures can be characterized by their time-dependent permeabilities, so that the evolution of the resulting fluid flow processes can be determined from permeability measurements under varied experimental conditions. Therefore, a comprehensive investigation of the time-dependent permeability of shale fractures is required to deeply understand the long-term safety and stability of the aforementioned underground projects.

The time-dependent behavior of the permeability induced by creep in porous rock under stress conditions has been extensively studied in many laboratory measurements (An et al. 2021; Guo et al. 2018; Liu et al. 2016a; Van Noort and Yarushina 2018). Steady-state permeability measurements on tight rocks under constant confining stress have shown that permeability declines significantly over time when all other variables remain constant (Chhatre et al. 2014; Sinha et al. 2013). Liu et al. (2016b) divided the evolution process of the gas permeability of low-permeable claystone with time into four stages and described the relation between the permeability variation and volumetric strain. The corresponding mechanisms were explained as clay packing, grain rearrangement, and progressive collapse of the pore spaces (Chang and Zoback 2009; Sone and Zoback 2014). For fractures, the widely accepted reasons for the time-dependent variation in permeability include mechanical creep, clay swelling, and pressure solution (Elkhoury et al. 2015; Polak et al. 2003; Yasuhara et al. 2006; Zhang and Talandier 2022). Mechanical creep can affect the fracture void space and aperture distribution, which alters the hydraulic properties of the fracture. Clay swelling on the fracture surface can cause the aperture to decrease and thus change the permeability. Pressure solution, a chemo-mechanical process, is one of the important processes leading to diagenetic compaction and deformation in rocks (Kamali-Asl et al. 2018; Yasuhara 2004). The contacting asperities dissolve under high local stress, and the dissolved minerals diffuse from the high-stress regions to the less-stress regions based on

chemical potential and then precipitate on the free faces of the fracture surfaces. Among these three mechanisms, the latter two are applicable for water-saturated rocks where gas–water two-phase flow exists. Zhang (2013) conducted a series of laboratory flow-through experiments on fractured Callovo-Oxfordian argillite and Opalinus claystone, which can undergo significant self-sealing over time due to the combined effects of mechanical creep compaction and water-induced clay swelling, resulting in substantial permeability loss with time. Bandara et al. (2021) performed experimental investigations on propped siltstone fractures and found that creep-induced proppant embedment significantly affected fracture permeabilities, with a permeability reduction of up to 92% within 144 h, which can be roughly expressed as an exponential function. In addition to experimental studies, some permeability creep models have been established and developed to describe the time-dependent variations in permeability. Danesh et al. (2016) combined the Nishihara model and stress−strain constitutive equation to derive a new permeability model that captures the effect of inelastic deformation on coal permeability. Based on the creep strain equation and stress-dependent permeability model, An et al. (2021) proposed an improved permeability model considering the creep effects and validated it with experimental data from Chhatre et al. (2014). Kamali-Asl et al. (2020) used a three-element rheological model to calculate the variation in fracture aperture and predict the time-dependent evolution of fracture permeability. The permeability prediction model was valid during the test period for both the loading and unloading paths. Most existing permeability models tend to focus only on the creep effect, which works well, but is difficult to apply to the calculation of time-dependent gas permeability because of the gas slippage phenomenon.

Gas slippage is a common occurrence during gas transport in porous media, and it significantly affects the permeability of rocks (Gao et al. 2017; Li et al. 2018). When the pore radius for gas flow approaches the mean free flow path of gas molecules, collisions between the gas molecules and pore walls become more dominant than molecule-to-molecule collisions. At this time, gas molecules "slip" near the wall surfaces, promoting gas transport and producing additional fluxes (Chen et al. 2020; Klinkenberg 1941). Our previous studies have shown that gas flow in microscale fractures cannot be entirely described by Darcy flow, and gas slippage has a significant impact on gas flow (Cheng and Yu 2019, 2022). In recent years, despite extensive research on gas slippage, the understanding of how it varies with the time-dependent deformation of the fracture remains unclear. This makes it difficult to interpret time-dependent gas transport processes in fractured rocks. Additionally, most gas permeability models incorporate gas slippage contributions but do not consider the creep effect, which may lead to incorrect rock parameters. To our knowledge, the

time-dependent variation in the gas flow process in fractures has rarely been reported, and related experimental data are extremely limited. Considering the wide range of variation in the formation stress in long-term underground projects, it is critical to investigate the time-dependent behavior of gas permeability in fractures under multilevel confining stresses. This will help us better understand the gas transport processes in fractured shales. An effective permeability model that considers the coupling effect of creep and gas slippage is also required to predict the time-dependent evolution of fracture permeability for the long-term safety and stability of subsurface engineering.

In this study, two borehole core samples of shale were retrieved to experimentally investigate the time-dependent gas permeability of shale fractures under multilevel confining stresses. Each shale core contained a single fracture along its axis. Prior to the experiments, the mineral composition, pore distribution characteristics, and matrix permeability of the shale samples were measured. The surface topographies of the two fracture surfaces were reconstructed, and the aperture distribution and roughness of the fracture were analyzed. Steady-state gas flow tests were conducted with different gas pressures to measure the gas permeabilities of the fractures under multilevel confining stresses, and the associated apertures were calculated numerically. Based on the experimental data, the time-dependent behavior of the fracture permeability was analyzed, and the factors influencing the evolution of the gas transport process were discussed. The variation in the gas slippage effect caused by creep was also evaluated and quantified by a power function. Finally, a time-dependent gas permeability model of the fracture considering the coupling effect of creep and gas slippage was proposed and validated by experimental data. The variations in permeability over the next 30 days were predicted based on this model.

2 Description of the Samples

2.1 Properties of the Shale Matrix

Two shale core samples were acquired from the Carboniferous formation of the eastern Qaidam Basin in China. These samples were drilled into cylindrical cores from core plugs of the ZK1-1 well at depths of 494 m and 518.6 m. The mineral compositions of the samples were measured by X-ray diffraction (XRD) on the shale powder, and the results are shown in Table 1. The main nonclay minerals are quartz and calcite. The contents of clay minerals for Samples 1 and 2 are 46.6% and 36%, respectively, and the dominant clay minerals are mixed layer illite–smectite, illite, and kaolinite. The total organic carbon content was measured by a carbon–sulfur analyzer, and the results are also listed in Table 1. The pore distribution of the matrix was determined by high-pressure mercury intrusion porosimetry (MIP) and low-pressure adsorption of N_2 and CO_2. The measurement results are displayed in Fig. 1 and Table 2. The pore structure analysis shows that the proportions of pore sizes less than 50 nm account for 90% of the total pore size. The clear peak values in Fig. 1 indicate that the most dominant pore sizes for the two samples are approximately 34.33 and 25.25 nm. In addition, the average pore size, porosity, and bulk density of the shale samples were acquired and listed in Table 2.

The matrix permeabilities of the dry cores were measured by the steady-state flow method at a range of methane gas pressures. The gas apparent permeability (k_{app}) of the core sample can be calculated according to the modified Darcy's law:
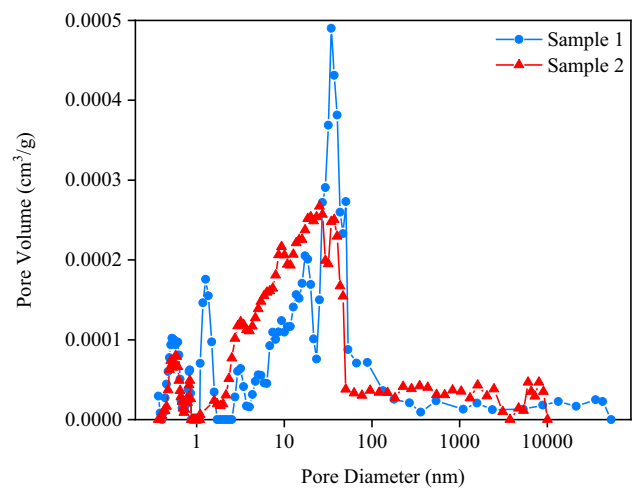

Fig. 1 Pore distribution of the shale matrix

Table 1 Mineral composition and mechanical parameters of the shale cores

Sample number	Nonclay minerals (%)						Clay minerals (%)				TOC (%)
	Q	Ca	Fel	Ank	Py	Fa	It	Ka	Ch	I/S	
1	47.4	0.9	1.7	–	3.4	–	6.8	18.1	4.5	17.2	3.05
2	44	12	3	2	1	2	12.6	8.3	4.3	10.8	0.59

Q quartz; *Ca* calcite; *Fel* feldspar; *Py* pyrite; *Ank* Ankerite; *Fa* Fayalite; *I* illite; *Ka* kaolinite; *Ch* chlorite; *I/S* illite−smectite mixed layer; *TOC* total organic carbon

Table 2 The dimensional specifications and elastic parameters of the samples

Sample number	Depth (m)	Diameter (cm)	Length (cm)	Bulk density (g/cm^3)	Porosity (%)	Average pore size (nm)	Young's modulus (GPa)	Poisson's ratio
1	494.00	4.98	4.72	2.56	2.99	11.36	24.66	0.163
2	518.60	4.90	4.80	2.47	6.27	16.82	33.14	0.203

The sample information of Sample 2 is cited from Cheng and Yu (2022)

Table 3 The gas flow test results of the intact samples before fracturing

| Sample 1					Sample 2				
P_1 (MPa)	P_2 (MPa)	Q (cm^3/s)	k_{app} (m^2)	k_{in} (m^2)	P_1 (MPa)	P_2 (MPa)	Q (cm^3/s)	k_{app} (m^2)	k_{in} (m^2)
0.401	0.097	4.44×10^{-4}	1.65×10^{-19}	1.16×10^{-20}	0.384	0.097	6.24×10^{-5}	2.46×10^{-20}	2.33×10^{-20}
0.704	0.097	1.26×10^{-3}	1.44×10^{-19}		0.493	0.097	1.04×10^{-4}	2.44×10^{-20}	
0.895	0.097	2.00×10^{-3}	1.41×10^{-19}		0.675	0.097	1.97×10^{-4}	2.41×10^{-20}	
1.106	0.097	2.96×10^{-3}	1.36×10^{-19}		0.973	0.097	4.09×10^{-4}	2.38×10^{-20}	

$$k_{app} = \frac{2P_0 \mu QLZ}{A(P_1^2 - P_2^2)Z_a}, \tag{1}$$

where P_0 is atmospheric pressure ($P_0 = 0.097$ MPa); μ is the gas dynamic viscosity; Q is the gas flow rate; L is the sample length; Z and Z_a are gas compressibility factors under the experimental temperature and pressure and the experimental temperature and atmospheric pressure, respectively; A is the cross-sectional area of the core sample; and P_1 and P_2 are the inlet and outlet gas pressures. The intrinsic permeability (k_{in}) was then obtained by using Klinkenberg's slip model to correct the gas apparent permeability (Klinkenberg 1941). The measured results are provided in Table 3.

2.2 Preparation and Microstructural Characteristic Measurement of the Fracture

The Brazilian fracturing method was used to artificially create a single rough fracture in each core. The corresponding details are described in Cheng and Yu (2019). The resulting fracture was appropriately located centrally and extended longitudinally along the axis throughout the core, as shown in Fig. 2. The elastic parameters of the fractured cores (the Young's modulus and Poisson's ratio) were measured by ultrasonic measurements, and the results are also presented in Table 2. Note that Sample 2 was used to conduct a series of gas percolation experiments, and the details are provided in Cheng and Yu (2022).

Fracture topography was measured using a high-precision three-dimensional (3-D) laser scanner with a scanning interval of 30 μm and a resolution of 7 μm. The scanned data were applied to reconstruct the fracture surfaces and
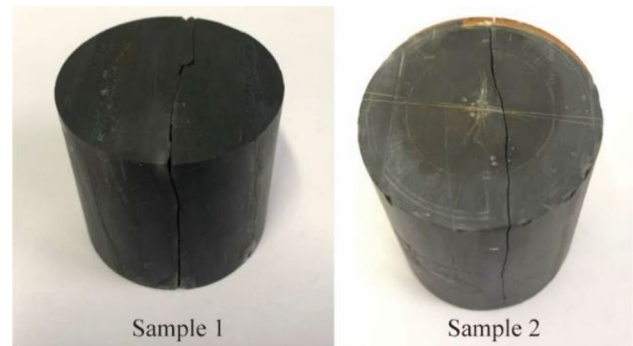
Fig. 2 Pictures of the fractured shale cores

calculate the morphology parameters of the fractures via digital processing, with details described below. First, GOM Inspect (a software for detailed evaluations of 3-D data) was used to align the two fracture surfaces to a common base plane, and the data were exported in a stereolithography (STL) file. Subsequently, the obtained STL files were imported into Surfer software to reconstruct the 3-D surfaces, as shown in Fig. 3, and then the data were converted to a GRID file, which includes the XYZ coordinates of the two surfaces, to calculate the roughness parameters.

The roughness of each fracture was characterized by the mean asperity height (R_m), root mean square of the asperity height (R_{rms}), and joint roughness coefficient (JRC), which were calculated as follows (Isaka et al. 2020; Sausse 2002; Tse and Cruden 1979):

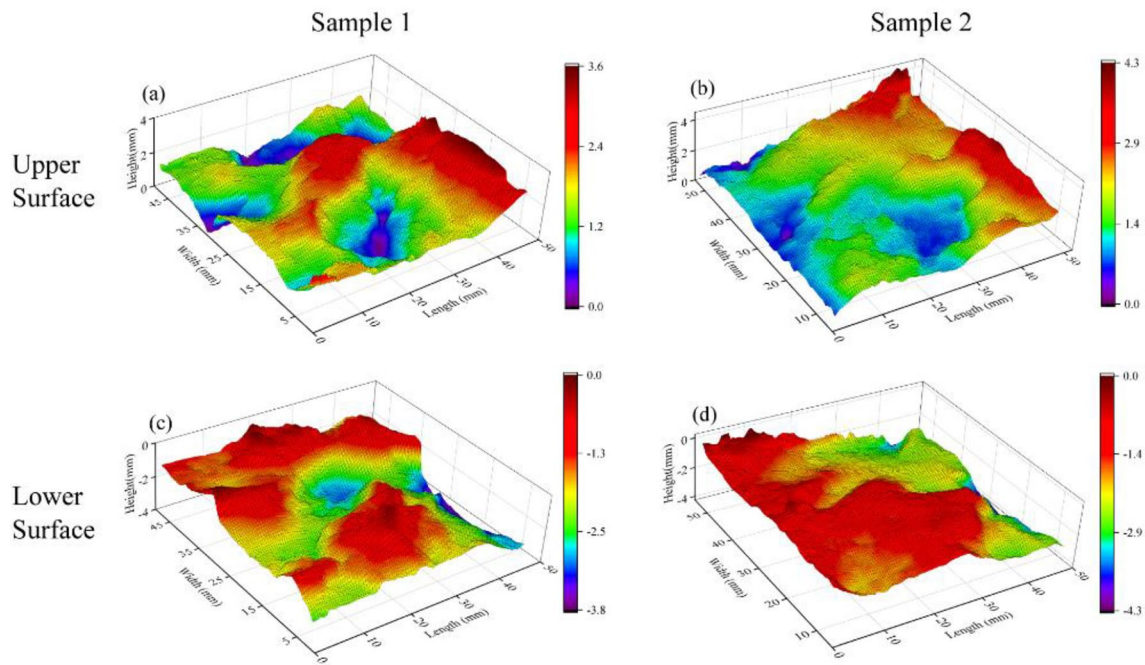$$R_m = \frac{1}{n} \sum_{i=1}^{n} |z_i - z_a|, \tag{2}$$

Fig. 3 Three-dimensional surface topography of the fracture

$$R_{\mathrm{rms}} = \sqrt{\frac{1}{n} \sum_{i=1}^{n} (z_i - z_a)^2}, \tag{3}$$

$$Z_2 = \left[\frac{1}{L} \sum_{i=1}^{n-1} \frac{(z_{i+1} - z_i)^2}{\Delta x} \right]^{0.5}, \tag{4a}$$

$$\mathrm{JRC} = 32.2 + 32.47 \times \log_{10} Z_2, \tag{4b}$$

where z_i is the asperity height at point i, z_a is the mean asperity height, and n is the number of total data points. Note that the 3-D profile of a fracture surface consists of multiple two-dimensional (2-D) profiles along the flow direction. These 2-D profiles were averaged to find the Z_2 and JRC values. The roughness parameters in Table 4 show that the values of R_m and R_{rms} for the two samples are approximately equal, but the JRC value of Sample 2 is larger than that of Sample 1, suggesting that the fracture surface of Sample 2 is rougher than that of Sample 1. According to the JRC value and the

mining rock mass rating classification system proposed by Milne (1990), the fracture surfaces of the two samples are slightly rough and can be classified as curved rough.

The fracture aperture was defined as the small gap between the two surfaces, which can be obtained by subtracting the elevation levels of the asperities at a particular location on the two surfaces, mathematically represented as follows:

$$e_{ij} = T_{ij} - B_{ij}, \tag{5a}$$

$$e_{ij} \geq 0, \tag{5b}$$

where e_{ij} is the aperture at given coordinates and T_{ij} and B_{ij} are the elevation levels of the asperities at coordinates (i, j) for the top and bottom surfaces, respectively. Based on Eq. (5b), the overlapping points on the fracture surfaces were identified, and the corresponding apertures were assigned a value of 0, which represents a zero fracture aperture (i.e., the contacted asperities). The contact area of the two fracture surfaces was calculated by the percentage of zero aperture points.

Table 4 The results of the geometrical parameters of the fracture surfaces

Sample	R_m (mm)	R_{rms} (mm)	Z_2	JRC	e_{ave} (mm)	e_{st} (mm)	A_c (%)
1	0.56	0.70	0.16	7.32	0.25	0.08	1.16
2	0.58	0.69	0.23	11.48	0.06	0.04	10.30

e_{ave}, average aperture; e_{st}, standard deviation of the aperture distribution; and A_c, contact area of the fracture surface

The distribution histograms of the fracture apertures are plotted in Fig. 4, along with the variations in the probability density of the corresponding normal distribution functions. The average apertures and the standard deviations of the aperture distribution are listed in Table 4. The results show that more than 95% of the apertures of Samples 1 and 2 are in the ranges of 0.12–0.5 mm and 0–0.14 mm, respectively, and the e_{ave} of Sample 1 is higher than that of Sample 2.

3 Methodology

3.1 Experimental Procedure

Our main experimental goal is to monitor the time-dependent variation in fracture permeability under multilevel confining stresses. The fracture permeabilities were measured by the steady-state flow method using methane gas. Four different confining stresses of 10, 15, 20, and 25 MPa were applied in the experiments. Considering the safe operation of the experimental apparatus as well as actual formation temperature, all experimental temperatures were set to 40 ℃.

This temperature also minimizes the influence of ambient temperature on the flow-through experiments.

A schematic of the experimental apparatus for the gas flow measurements is shown in Fig. 5. The core was wrapped in a fluororubber sleeve and placed into the core holder. To ensure that the core was evenly stressed, two cylindrical steel cores with diameters of 5 cm were placed at both ends of the shale core. A syringe pump with a maximum capacity of 50 MPa was used to apply the confining stress to the cores to simulate in situ formation conditions. The fluid injection system was connected to the core holder and could inject gas into the sample at a constant pressure. The inlet and outlet pressures at both ends of the sample were monitored by two high-precision pressure gauges (0–20 MPa, ± 0.1 kPa). A gas flow meter at the outlet was used to measure the gas volume flow rate. All experimental devices and pipelines were thermostatically controlled in a thermostat (± 0.05 ℃).

The experimental procedure was as follows. Prior to testing, the samples were oven dried at 105 ℃ for 8 h. The dry core and two steel cores were placed into the core holder, a confining stress of 10 MPa was applied to the cores, and the entire system was vacuumed and leak-tested. Subsequently, methane was injected into the core holder. The
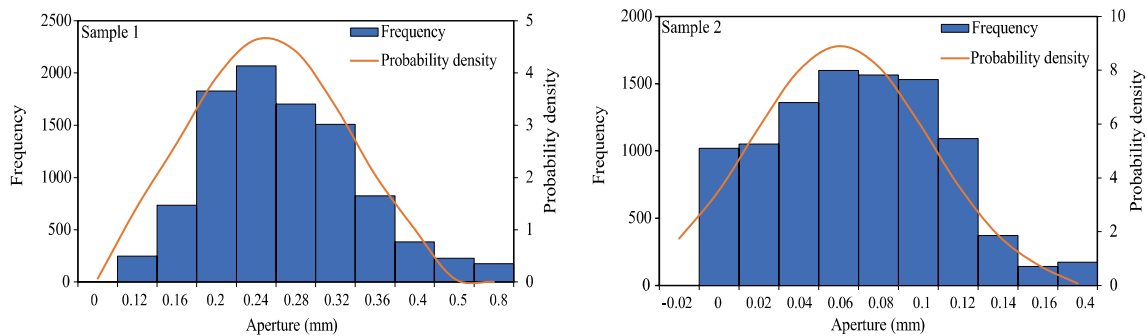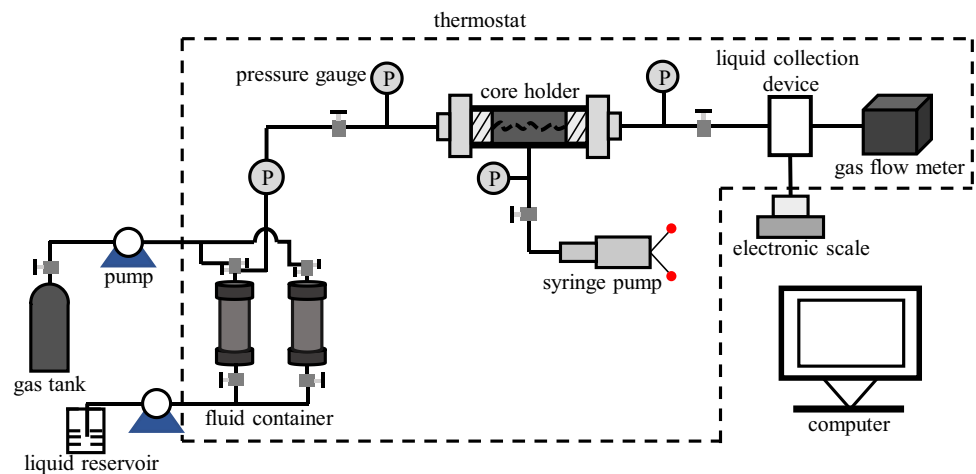

Fig. 4 Frequency distribution histogram and corresponding normal distribution curve of the fracture aperture

Fig. 5 Schematic diagram of the apparatus for the gas permeability measurements

inlet pressures, outlet pressures at both ends of the core, and gas volume flow rates were recorded and used to calculate the permeability. To improve the accuracy of the gas permeability, the gas flow rates were measured three times under each inlet pressure to ensure that steady-state flow was achieved. The gas permeabilities were measured every 24 h for 14 days. The confining stress was maintained at a constant 10 MPa during this period and then loaded to the next level. At later confining stress levels (15, 20, and 25 MPa), the duration of the permeability measurement was shortened from 14 days to 7 days. The confining stress was monotonically increased in steps of 5 MPa from 10 to 25 MPa and then unloaded in 5 MPa steps from 25 to 10 MPa at a rate of 0.2 MPa/min during all the loading and unloading processes. Note that each level of confining stress lasted only 2 days during unloading. The specific test path is illustrated in Fig. 6.

3.2 Determination of the Fracture Permeability and Aperture

Comparing the flow rates of the cores before and after fracturing under the same gas pressure, we found that the gas flow rates of the fractured cores were three orders of magnitude higher than those of the cores before fracturing. This suggests that the gas flow in the matrix is negligible compared to the total flow in the fractured cores and that all pressure and flow measurements directly reflected the fracture properties. Similar to the matrix, Darcy's law (Eq. (1)) was used to calculate the apparent permeability of the fracture. Due to the high-velocity gas flow in the fracture, however, the applicability of Darcy's law should first be demonstrated based on the Reynolds number (Rathnaweera et al. 2015), which is given by (Chen et al. 2015; Ranjith and Darlington 2007):

Fig. 6 Loading and unloading path in the experimental run

$$Re = \frac{\rho v e_h}{\mu} = \frac{\rho Q}{\mu w}, \tag{6}$$

where ρ and ν are the density and flow velocity of the fluid, respectively, and e_h is the hydraulic aperture, which is defined as the aperture of a smooth fracture generating the same volumetric flow as the rough fracture. With the knowledge that the fluid flow rate of the fracture $Q = A_f \nu$ and the cross-sectional area of the fracture $A_f = e_h w$, Re can be rewritten as the second equation in Eq. (6), where w is the width of the fracture along the cross-section and is equal to the core's diameter. The Reynolds number (Re) at all experimental conditions were calculated and listed in Table 5. The Re are in the range of 1.6–219.7, indicating that the methane flow behaves as a laminar flow, and Darcy's law can be applied to calculate the apparent permeability for fractured shale samples. For fracture, Eq. (1) can thus be rewritten as:

$$Q = \frac{k_{app}A_f(P_1^2 - P_2^2)Z_a}{2\mu P_o L Z} = \frac{k_{app}e_h w(P_1^2 - P_2^2)Z_a}{2\mu P_o L Z}. \tag{7}$$

According to the cubic law of gas flow in a smooth fracture, Q can be determined as follows (Witherspoon et al. 1980):

$$Q = \frac{e_h^3}{12\mu L}\frac{w(P_1^2 - P_2^2)Z_a}{2P_o Z}. \tag{8}$$

Combining Eqs. (7) and (8), the apparent fracture permeability and hydraulic aperture can be derived as follows (Cheng and Yu 2022):

$$k_{app} = \frac{1}{12}\left(\frac{12\mu QZ}{wZ_a}\frac{2P_0 L}{P_1^2 - P_2^2}\right)^{\frac{2}{3}}, \tag{9}$$

$$e_h = \sqrt[3]{\frac{24\mu QZP_0 L}{(P_1^2 - P_2^2)wZ_a}}. \tag{10}$$

Since the mechanical aperture of the fracture cannot be directly measured during our experiments, a numerical method named the interpenetration model was performed based on the digital data of fracture surface topography to determine the variation in mechanical aperture associated with the time-dependent fracture permeability. The interpenetration model assumed a perfectly plastic rock response. All local apertures of the fracture were uniformly reduced based on the two surfaces being displaced relative to each other. The overlapping parts of the contacting asperities were removed, and the apertures at these points were set as 0.03 μm. Although this model is relatively simple, it is effective and agrees quite well with the results of flow tests (Cardona et al. 2021; Cheng and Milsch 2021; Deng et al.
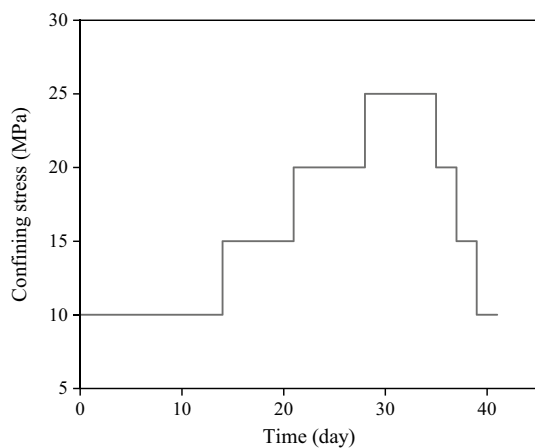
Table 5 The measurement results of the gas permeability under experimental conditions

Sample1							Sample 2						
P_C (MPa)	Time (day)	P_1 (MPa)	P_2 (MPa)	Q (cm³/s)	k_{app} (10^{-13} m²)	Re	P_C (MPa)	Time (day)	P_1 (MPa)	P_2 (MPa)	Q (cm³/s)	k_{app} (10^{-13} m²)	Re
10 MPa	0	0.597	0.097	6.054	48.974	22.469	10 MPa	0	0.597	0.097	1.247	17.069	4.629
		0.897	0.097	11.955	44.335	63.575			0.897	0.097	2.489	15.558	13.233
		1.297	0.097	21.285	39.655	158.810			1.097	0.097	3.530	14.972	22.553
		1.497	0.097	25.750	37.180	219.740			1.297	0.097	4.745	14.554	35.403
	1	0.597	0.097	4.224	38.524	15.676		1	0.597	0.097	0.634	10.866	2.351
		0.897	0.097	8.558	35.478	45.511			0.897	0.097	1.314	10.165	6.990
		1.297	0.097	15.294	31.813	114.111			1.097	0.097	1.895	9.890	12.109
		1.497	0.097	18.352	29.639	156.606			1.297	0.097	2.582	9.700	19.262
	2	0.597	0.097	3.938	36.765	14.614		2	0.597	0.097	0.578	10.224	2.146
		0.897	0.097	8.021	33.976	42.652			0.897	0.097	1.216	9.654	6.469
		1.297	0.097	14.409	30.573	107.508			1.097	0.097	1.769	9.448	11.305
		1.497	0.097	17.297	28.492	147.606			1.297	0.097	2.415	9.277	18.015
	3	0.597	0.097	3.739	35.517	13.876		3	0.597	0.097	0.532	9.673	1.975
		0.897	0.097	7.698	33.060	40.938			0.897	0.097	1.133	9.208	6.026
		1.297	0.097	13.807	29.716	103.017			1.097	0.097	1.658	9.047	10.594
		1.497	0.097	16.593	27.713	141.594			1.297	0.097	2.269	8.901	16.931
	4	0.597	0.097	3.618	34.747	13.428		4	0.597	0.097	0.486	9.107	1.804
		0.897	0.097	7.496	32.478	39.863			0.897	0.097	1.040	8.698	5.532
		1.297	0.097	13.449	29.199	100.342			1.097	0.097	1.526	8.559	9.748
		1.497	0.097	16.171	27.242	137.999			1.297	0.097	2.091	8.428	15.600
	5	0.597	0.097	3.523	34.134	13.074		5	0.597	0.097	0.476	8.978	1.766
		0.897	0.097	7.295	31.895	38.794			0.897	0.097	1.021	8.592	5.432
		1.297	0.097	13.127	28.732	97.945			1.097	0.097	1.500	8.461	9.582
		1.497	0.097	15.783	26.804	134.687			1.297	0.097	2.057	8.337	15.349
	6	0.597	0.097	3.468	33.779	12.871		6	0.597	0.097	0.467	8.862	1.732
		0.897	0.097	7.172	31.536	38.140			0.897	0.097	1.004	8.492	5.337
		1.297	0.097	12.956	28.482	96.667			1.097	0.097	1.473	8.359	9.409
		1.497	0.097	15.574	26.567	132.901			1.297	0.097	2.024	8.248	15.103
	7	0.597	0.097	3.404	33.360	12.632		7	0.597	0.097	0.462	8.801	1.714
		0.897	0.097	7.033	31.125	37.398			0.897	0.097	0.990	8.417	5.266
		1.297	0.097	12.794	28.244	95.461			1.097	0.097	1.455	8.291	9.294
		1.497	0.097	15.376	26.341	131.211			1.297	0.097	1.993	8.164	14.872
	8	0.597	0.097	3.380	33.203	12.543		8	0.597	0.097	0.455	8.715	1.689
		0.897	0.097	6.985	30.984	37.144			0.897	0.097	0.979	8.354	5.207
		1.297	0.097	12.672	28.063	94.545			1.097	0.097	1.440	8.237	9.203
		1.497	0.097	15.230	26.174	129.964			1.297	0.097	1.976	8.116	14.741
	9	0.597	0.097	3.347	32.986	12.420		9	0.597	0.097	0.451	8.666	1.675
		0.897	0.097	6.910	30.764	36.747			0.897	0.097	0.971	8.309	5.166
		1.297	0.097	12.529	27.852	93.477			1.097	0.097	1.431	8.200	9.142
		1.497	0.097	15.057	25.975	128.487			1.297	0.097	1.961	8.075	14.630
	10	0.597	0.097	3.308	32.734	12.278		10	0.597	0.097	0.445	8.588	1.652
		0.897	0.097	6.861	30.618	36.488			0.897	0.097	0.963	8.261	5.121
		1.297	0.097	12.426	27.700	92.715			1.097	0.097	1.418	8.152	9.061
		1.497	0.097	14.940	25.841	127.496			1.297	0.097	1.950	8.046	14.551
	11	0.597	0.097	3.303	32.700	12.318		11	0.597	0.097	0.442	8.546	1.640
		0.897	0.097	6.813	30.474	36.346			0.897	0.097	0.960	8.243	5.104
		1.297	0.097	12.364	27.607	92.331			1.097	0.097	1.417	8.146	9.051

Table 5 (continued)

Sample1							Sample 2						
P_C (MPa)	Time (day)	P_1 (MPa)	P_2 (MPa)	Q (cm³/s)	k_{app} (10⁻¹³ m²)	Re	P_C (MPa)	Time (day)	P_1 (MPa)	P_2 (MPa)	Q (cm³/s)	k_{app} (10⁻¹³ m²)	Re
		1.497	0.097	14.859	25.747	126.799			1.297	0.097	1.950	8.044	14.546
	12	0.597	0.097	3.271	32.489	12.185		12	0.597	0.097	0.444	8.532	1.646
		0.897	0.097	6.761	30.319	36.092			0.897	0.097	0.956	8.224	5.086
		1.297	0.097	12.291	27.492	92.195			1.097	0.097	1.408	8.113	8.996
		1.497	0.097	14.792	25.669	126.225			1.297	0.097	1.933	7.997	14.420
	13	0.597	0.097	3.256	32.394	12.184		13	0.597	0.097	0.440	8.521	1.633
		0.897	0.097	6.752	30.290	35.965			0.897	0.097	0.950	8.188	5.053
		1.297	0.097	12.256	27.468	91.616			1.097	0.097	1.403	8.092	8.962
		1.497	0.097	14.760	25.633	125.833			1.297	0.097	1.923	7.969	14.344
	14	0.597	0.097	3.243	32.300	15.676		14	0.597	0.097	0.435	8.460	1.615
		0.897	0.097	6.742	30.262	45.511			0.897	0.097	0.944	8.154	5.021
		1.297	0.097	12.254	27.443	114.111			1.097	0.097	1.395	8.063	8.914
		1.497	0.097	14.746	25.616	156.606			1.297	0.097	1.916	7.952	14.298
15 MPa							15 MPa						
	14	0.597	0.097	2.367	26.098	8.801		14	0.897	0.097	0.582	5.906	3.103
		0.897	0.097	5.033	24.750	26.880			1.097	0.097	0.860	5.851	5.513
		1.297	0.097	9.283	22.776	69.425			1.297	0.097	1.179	5.780	8.805
		1.497	0.097	11.161	21.276	95.241			1.497	0.097	1.539	5.701	13.139
	15	0.597	0.097	2.086	23.911	7.755		15	0.897	0.097	0.524	5.516	2.796
		0.897	0.097	4.553	23.211	24.317			1.097	0.097	0.780	5.485	4.999
		1.297	0.097	8.483	21.485	63.443			1.297	0.097	1.071	5.425	8.002
		1.497	0.097	10.248	20.094	87.455			1.497	0.097	1.403	5.356	11.977
	16	0.597	0.097	2.018	23.562	7.504		16	0.897	0.097	0.514	5.458	2.744
		0.897	0.097	4.483	22.980	23.943			1.097	0.097	0.766	5.409	4.907
		1.297	0.097	8.385	21.230	62.709			1.297	0.097	1.055	5.356	7.877
		1.497	0.097	10.089	19.886	86.098			1.497	0.097	1.377	5.301	11.757
	17	0.597	0.097	1.983	23.216	7.376		17	0.897	0.097	0.507	5.396	2.705
		0.897	0.097	4.403	22.584	23.513			1.097	0.097	0.756	5.367	4.843
		1.297	0.097	8.180	20.932	61.172			1.297	0.097	1.038	5.315	7.750
		1.497	0.097	9.863	19.592	84.163			1.497	0.097	1.362	5.248	11.629
	18	0.597	0.097	1.952	22.982	7.260		18	0.897	0.097	0.504	5.375	2.691
		0.897	0.097	4.322	22.445	23.083			1.097	0.097	0.750	5.337	4.808
		1.297	0.097	8.117	20.814	60.700			1.297	0.097	1.029	5.288	7.688
		1.497	0.097	9.787	19.491	83.518			1.497	0.097	1.354	5.232	11.559
	19	0.597	0.097	1.940	22.886	7.215		19	0.897	0.097	0.496	5.328	2.647
		0.897	0.097	4.300	22.349	22.964			1.097	0.097	0.737	5.291	4.721
		1.297	0.097	8.050	20.747	60.202			1.297	0.097	1.018	5.243	7.600
		1.497	0.097	9.729	19.414	83.024			1.497	0.097	1.336	5.189	11.407
	20	0.597	0.097	1.930	22.777	7.178		20	0.897	0.097	0.497	5.316	2.651
		0.897	0.097	4.283	22.230	22.875			1.097	0.097	0.738	5.282	4.731
		1.297	0.097	8.013	20.666	59.925			1.297	0.097	1.017	5.239	7.594
		1.497	0.097	9.675	19.342	82.561			1.497	0.097	1.334	5.180	11.393
	21	0.597	0.097	1.917	22.527	7.127		21	0.897	0.097	0.495	5.309	2.641
		0.897	0.097	4.233	22.126	22.610			1.097	0.097	0.733	5.275	4.694
		1.297	0.097	7.950	20.569	59.454			1.297	0.097	1.011	5.224	7.551
		1.497	0.097	9.616	19.264	82.062			1.497	0.097	1.325	5.166	11.316

Table 5 (continued)

Sample1							Sample 2						
P_C (MPa)	Time (day)	P_1 (MPa)	P_2 (MPa)	Q (cm³/s)	k_{app} (10^{-13} m²)	Re	P_C (MPa)	Time (day)	P_1 (MPa)	P_2 (MPa)	Q (cm³/s)	k_{app} (10^{-13} m²)	Re
20 MPa							20 MPa						
	21	0.897	0.097	3.069	17.857	16.319		21	1.297	0.097	0.714	4.119	5.328
		1.297	0.097	5.901	16.841	44.031			1.497	0.097	0.941	4.080	8.045
		1.497	0.097	7.472	16.277	63.760			1.697	0.097	1.191	4.037	11.452
	22	0.897	0.097	2.687	16.325	14.287			1.897	0.097	1.464	3.983	15.672
		1.297	0.097	5.268	15.607	39.304		22	1.297	0.097	0.654	3.872	4.882
		1.497	0.097	6.719	15.150	57.338			1.497	0.097	0.855	3.838	7.310
	23	0.897	0.097	2.639	16.144	14.034			1.697	0.097	1.087	3.795	10.450
		1.297	0.097	5.183	15.435	38.674			1.897	0.097	1.333	3.755	14.268
		1.497	0.097	6.600	14.976	56.322		23	1.297	0.097	0.640	3.831	4.779
	24	0.897	0.097	2.586	15.947	13.751			1.497	0.097	0.842	3.797	7.197
		1.297	0.097	5.086	15.274	37.946			1.697	0.097	1.069	3.761	10.276
		1.497	0.097	6.501	14.846	55.477			1.897	0.097	1.318	3.716	14.112
	25	0.897	0.097	2.584	15.875	13.742		24	1.297	0.097	0.630	3.790	4.705
		1.297	0.097	5.070	15.224	37.826			1.497	0.097	0.833	3.765	7.115
		1.497	0.097	6.453	14.770	55.064			1.697	0.097	1.053	3.724	10.123
	26	0.897	0.097	2.551	15.806	13.566			1.897	0.097	1.297	3.686	13.881
		1.297	0.097	5.043	15.154	37.623		25	1.297	0.097	0.625	3.770	4.667
		1.497	0.097	6.450	14.717	55.042			1.497	0.097	0.826	3.744	7.056
	27	0.897	0.097	2.553	15.715	13.577			1.697	0.097	1.045	3.704	10.048
		1.297	0.097	5.020	15.075	37.453			1.897	0.097	1.286	3.665	13.765
		1.497	0.097	6.410	14.647	54.702		26	1.297	0.097	0.624	3.763	4.659
	28	0.897	0.097	2.500	15.609	13.294			1.497	0.097	0.820	3.727	7.008
		1.297	0.097	4.967	15.001	37.057			1.697	0.097	1.038	3.691	9.985
		1.497	0.097	6.351	14.573	54.198			1.897	0.097	1.281	3.650	13.712
25 MPa								27	1.297	0.097	0.618	3.748	4.613
	28	0.897	0.097	1.935	13.152	10.288			1.497	0.097	0.817	3.721	6.985
		1.297	0.097	3.923	12.809	29.269			1.697	0.097	1.037	3.684	9.973
		1.497	0.097	5.036	12.504	42.972			1.897	0.097	1.275	3.645	13.647
	29	0.897	0.097	1.702	12.060	9.048		28	1.297	0.097	0.616	3.728	4.600
		1.297	0.097	3.483	11.859	25.990			1.497	0.097	0.816	3.707	6.971
		1.497	0.097	4.532	11.640	38.671			1.697	0.097	1.033	3.666	9.931
	30	0.897	0.097	1.666	11.887	8.858			1.897	0.097	1.267	3.629	13.561
		1.297	0.097	3.452	11.752	25.759	25 MPa						
		1.497	0.097	4.467	11.523	38.123		28	1.297	0.097	0.462	3.084	3.450
	31	0.897	0.097	1.635	11.742	8.693			1.497	0.097	0.611	3.065	5.223
		1.297	0.097	3.400	11.656	25.368			1.697	0.097	0.777	3.035	7.472
		1.497	0.097	4.416	11.448	37.684			1.897	0.097	0.956	3.001	10.232
	32	0.897	0.097	1.617	11.655	8.597		29	1.297	0.097	0.431	2.931	3.214
		1.297	0.097	3.368	11.575	25.132			1.497	0.097	0.569	2.914	4.861
		1.497	0.097	4.367	11.350	37.270			1.697	0.097	0.725	2.892	6.968
	33	0.897	0.097	1.617	11.637	8.597			1.897	0.097	0.891	2.866	9.541
		1.297	0.097	3.352	11.537	25.011		30	1.297	0.097	0.419	2.881	3.127
		1.497	0.097	4.332	11.318	36.965			1.497	0.097	0.554	2.872	4.738
	34	0.897	0.097	1.600	11.566	8.508			1.697	0.097	0.707	2.851	6.798
		1.297	0.097	3.318	11.461	24.756			1.897	0.097	0.873	2.824	9.341
		1.497	0.097	4.300	11.248	36.694		31	1.297	0.097	0.415	2.866	3.100
	35	0.897	0.097	1.583	11.472	8.419			1.497	0.097	0.550	2.852	4.704

Table 5 (continued)

Sample1							Sample 2						
P_C (MPa)	Time (day)	P_1 (MPa)	P_2 (MPa)	Q (cm³/s)	k_{app} (10^{-13} m²)	Re	P_C (MPa)	Time (day)	P_1 (MPa)	P_2 (MPa)	Q (cm³/s)	k_{app} (10^{-13} m²)	Re
		1.297	0.097	3.302	11.421	24.639			1.697	0.097	0.700	2.831	6.731
		1.497	0.097	4.267	11.187	36.410			1.897	0.097	0.863	2.810	9.238
20 MPa								32	1.297	0.097	0.410	2.841	3.056
	35	0.897	0.097	1.652	11.823	8.785			1.497	0.097	0.545	2.829	4.658
		1.297	0.097	3.450	11.775	25.741			1.697	0.097	0.692	2.810	6.652
	36	0.897	0.097	1.667	11.878	8.865			1.897	0.097	0.855	2.786	9.156
		1.297	0.097	3.467	11.798	25.868		33	1.297	0.097	0.406	2.828	3.029
	37	0.897	0.097	1.678	11.932	8.923			1.497	0.097	0.539	2.817	4.607
		1.297	0.097	3.472	11.809	25.905			1.697	0.097	0.686	2.796	6.596
15 MPa						10.104			1.897	0.097	0.848	2.772	9.076
	37	0.897	0.097	1.900	12.979	29.225		34	1.297	0.097	0.404	2.809	3.011
		1.297	0.097	3.917	12.820	10.279			1.497	0.097	0.532	2.794	4.548
	38	0.897	0.097	1.933	13.159	29.464			1.697	0.097	0.680	2.779	6.539
		1.297	0.097	3.949	12.899	10.380			1.897	0.097	0.840	2.756	8.996
	39	0.897	0.097	1.952	13.244	29.531		35	1.297	0.097	0.401	2.801	2.990
		1.297	0.097	3.958	12.918	13.401			1.497	0.097	0.532	2.789	4.547
10 MPa						38.067			1.697	0.097	0.677	2.771	6.511
	39	0.897	0.097	2.520	15.643	13.746			1.897	0.097	0.837	2.747	8.956
		1.297	0.097	5.102	15.288	38.223	20 MPa						
	40	0.897	0.097	2.585	15.906	13.890		35	1.297	0.097	0.432	2.947	3.226
		1.297	0.097	5.123	15.329	38.253		36	1.297	0.097	0.435	2.957	3.249
	41	0.897	0.097	2.612	16.018	8.785		37	1.297	0.097	0.435	2.960	3.249
		1.297	0.097	5.127	15.348	25.741	15 MPa						
								37	1.297	0.097	0.505	3.268	3.772
								38	1.297	0.097	0.508	3.278	3.794
								39	1.297	0.097	0.509	3.279	3.802
							10 MPa						
								39	1.297	0.097	0.707	4.091	5.280
								40	1.297	0.097	0.721	4.139	5.385
								41	1.297	0.097	0.724	4.154	5.407

2021; Watanabe et al. 2008). Meanwhile, a local cubic law (LCL)-based flow-through simulation was conducted under the same boundary conditions as the seepage experiment to model the single-phase gas flow in a 2-D field while the aperture distribution changed. In the flow simulation, the equation of continuity (Reynolds equation) for the steady-state laminar flow was used (Nemoto et al. 2009; Yeo et al. 1998):

$$\frac{\partial}{\partial x}\left(\rho\frac{ek_g}{\mu}\frac{\partial P}{\partial x}\right) + \frac{\partial}{\partial y}\left(\rho\frac{ek_g}{\mu}\frac{\partial P}{\partial y}\right) = 0, \tag{11}$$

where P is the gas pressure, μ and ρ are the viscosity and density of the gas, which are functions of the gas pressure and can be acquired using REFPROP software, e is the local aperture, and k_g is the local gas permeability considering

the slippage effect in the fracture, which can be expressed as follows (Cheng and Yu 2022; Wang et al. 2019; Zaouter et al. 2018):

$$k_g = \frac{e^2}{12}\left(1 + 6\frac{\lambda\zeta}{e}\right), \tag{12}$$

where λ is the mean free path of the methane molecules ($\lambda = \frac{k_B T}{\sqrt{2}\pi\delta^2}$, where k_B is the Boltzmann constant and δ is the collision diameter of the gas molecule) and ζ is the slip factor ($\zeta = \frac{2-\sigma_v}{\sigma_v}$, where σ_v is the tangential momentum accommodation coefficient and assumed to be 0.75 in this study). Note that the permeability is invalid and the gas pressure cannot be defined at the location where the fracture aperture is zero (Watanabe et al. 2008). Considering that the most

dominant pore size of our two samples is approximately 0.03 µm (Fig. 1), we set the apertures at the contacting asperities to 0.03 µm for this analysis.

Constant gas pressures were applied at the boundary perpendicular to the direction of macroscopic flow. The boundary parallel to the macroscopic flow direction was assigned a no-flow boundary. By solving the finite difference form of Eq. (11), the velocity field was determined. The outlet flow rate can thus be calculated as follows:

$$Q = \int_0^w eV dx, \tag{13}$$

where e and V are the aperture and flow velocity in each grid at the outlet boundary, respectively, and w is the length of the outlet boundary (i.e., fracture width). By comparing and matching the experimentally and numerically derived flow rates, the mean mechanical aperture e_m can be obtained for prescribed confining stresses and times and expressed as follows:

$$e_m = \frac{1}{wL} \iint e\, dx\, dy. \tag{14}$$

4 Experimental Results

The experimental duration for the two samples was 41 days. Table 5 presents the apparent gas permeabilities k_{app} at different gas pressures and multilevel confining stresses P_c over the experimental period. The results show that k_{app} decreases significantly in Samples 1 and 2, up to 3.8 and 5.2 times, respectively, within the experimental gas pressure and confining stress ranges due to the elastic deformation and creep of the fracture. For simplicity, the experimental results at a gas pressure difference of 1.297 MPa are taken as a representative for analysis.

4.1 Time-Dependent Variation in the Fracture Permeability

The variations in apparent gas permeabilities of fractures under multilevel confining stresses are presented in Fig. 7a and b. To quantify the reduction in k_{app}, the permeability variations relative to the initial permeability are calculated and presented in Fig. 7c. Under a constant P_c of 10 MPa, k_{app} initially experiences a notable decrease over time. After four days, significant reductions of 26% and 42% are observed in the k_{app} of Samples 1 and 2, respectively. With increasing testing time, the rate of permeability reduction decreases. As P_c increases, k_{app} exhibits an instantaneous drop and

Fig. 7 Time-dependent fracture gas permeability of (**a**) Sample 1 and (**b**) Sample 2 at multilevel confining stresses and the cumulative reduction in gas permeability with (**c**) time and (**d**) confining stress
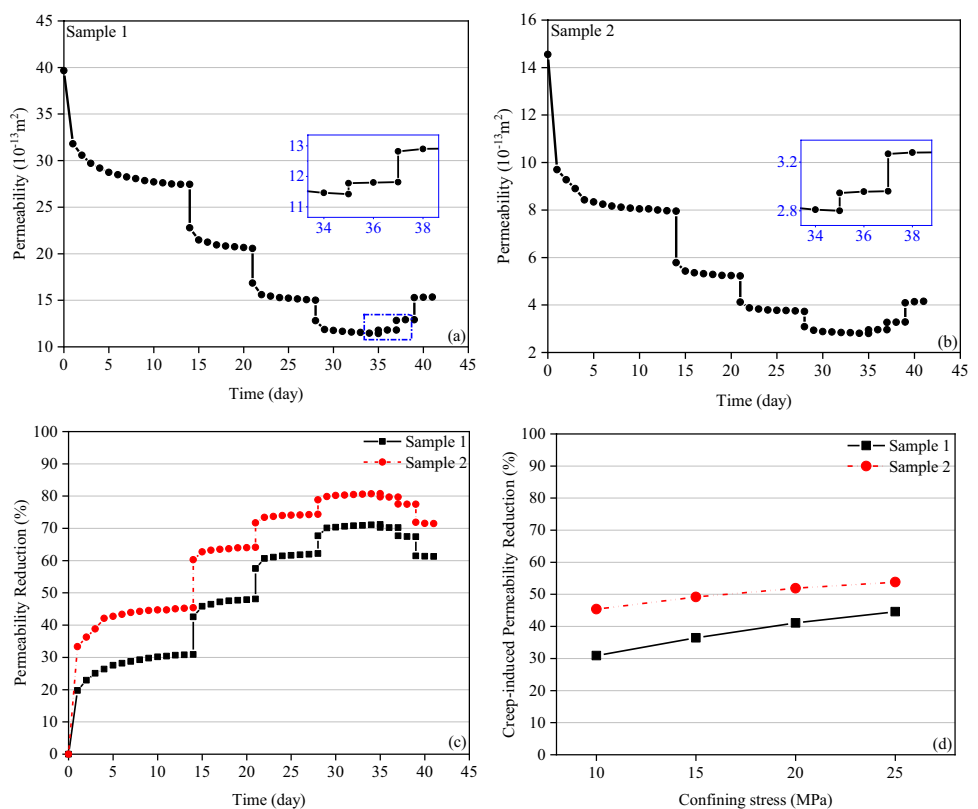
then manifests the same time-dependent reduction as that at the previous confining stress, but the variation amplitude is smaller than that in the previous stress stage. The time-dependent k_{app} variation at each stress level can be roughly divided into two stages: the decelerating decline stage with a rapid rate and the steady decline stage with a slow rate. The rapid and decelerating decline stage mainly lasts 4–5 days when the samples are initially subjected to a confining stress of 10 MPa. With increasing P_c, the duration of the first stage shortens to 1–2 days within each subsequent stress level. The shorter duration of the rapid and decelerating decline stage at higher confining stresses can be attributed to changes in the mechanical properties and microstructure of the fracture.

Figure 7d presents that the cumulative reduction in k_{app} caused by creep rises with increasing P_c, and at P_c values of 10, 15, 20, and 25 MPa, it reaches 30.90%, 36.47%, 41.11%, and 44.61% in Sample 1 and 45.36%, 49.18%, 51.87%, and 53.82% in Sample 2, respectively, but the increment of change decreases with increasing P_c. For clarity, the amounts of permeability reduction (Δk) caused by creep (Δk_c) and elastic deformation (Δk_i) during each confining stress stage are calculated separately and compared in Fig. 8. Notably, Δk_c at 10 MPa is significantly higher than all other values. As P_c increases from 10 to 25 MPa, both Δk_c and Δk_i gradually decrease, particularly Δk_i. However, the ratio of Δk_c to Δk_i rises with increasing P_c by up to 63.33% and 44.01% in Samples 1 and 2, respectively. In addition, the variations in the fracture permeability during the unloading phase are also monitored at the different confining stresses. It is observed in Fig. 7

Fig. 8 The amount of permeability reduction caused by elastic deformation and creep during each confining stress stage

that there is a slight recovery and irreversible reduction in permeability during the unloading process, and the permeability loss can be up to 71%. The recovery of permeability appears to increase with increasing stress drop. However, such a recovery process lasts only 1–2 days, and the magnitude and rate of permeability variations during this recovery process are much less than those monitored in the loading steps. Combined with Fig. 8, the permeability recovery mainly relies on the elastic recovery, while the time-dependent variation in permeability during this process is negligible.

4.2 Changes in Fracture Aperture

Note that mechanical apertures were not calculated for the entire duration of the experiment due to slight changes in permeability at the end of each loading stage and the negligible role of time-dependent permeability variation during the unloading phases. Only the evolution of mechanical apertures and hydraulic apertures of Samples 1 and 2 with time during the loading process is presented in Fig. 9. The initial mechanical apertures of Samples 1 and 2 under unconfined conditions are 249.9 and 58.2 μm, respectively. After being subjected to a confining stress of 10 MPa, the mechanical and hydraulic aperture of Samples 1 and 2 are reduced to 46.9 and 6.9 μm and 20.9 and 4.2 μm, respectively. Under the constant confining stress, the fracture aperture initially changes drastically with time and then starts converging. Larger aperture variations are observed at the initial loading (10 MPa), which decreases at higher confining stresses. At the end of the loading phase, the mechanical and hydraulic apertures are reduced to 42.3 and 3.7 μm for Sample 1, and to 17.2 and 1.8 μm for Sample 2, and fractures are still not fully closed. The comparison of aperture changes in Fig. 9c show that the change magnitudes of the mechanical aperture are larger than that of the hydraulic aperture, especially at high confining stress levels.

The variations in the contact area during the loading process are also presented in Fig. 10. The initial unstressed contact areas of Samples 1 and 2 are 1.16% and 10.3%, respectively. After being subjected to the confining stress, the contact area of Samples 1 and 2 increases drastically to 39.7% and 44.1%, respectively, reaching 44.1% and 50.2% at the end of the loading phase, respectively. The contact area first rises and then stabilizes with time at each confining stress. The overall variation in the contact area of Sample 2 is greater than that of Sample 1 due to the difference in aperture distribution.
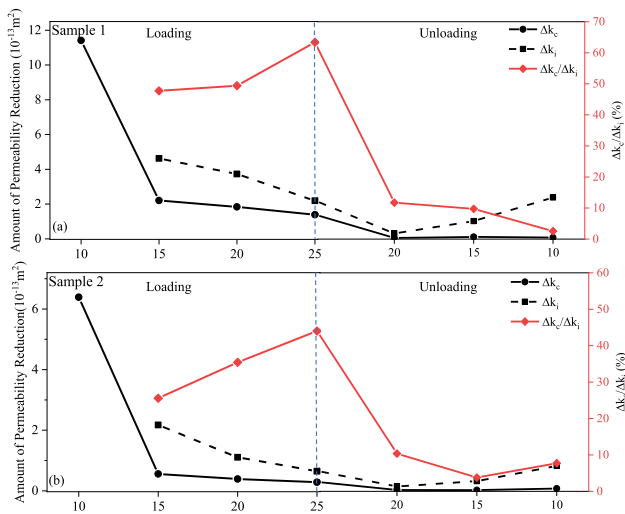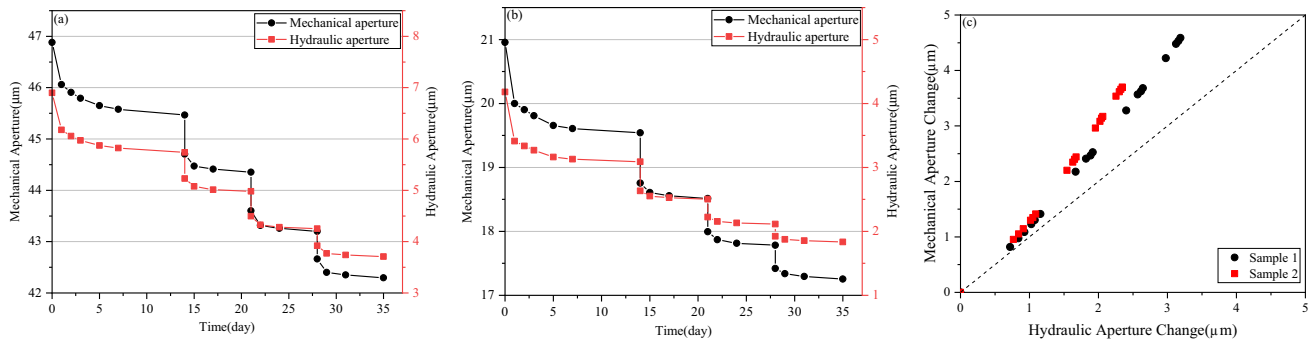
Fig. 9 The variations in the mechanical and hydraulic apertures of (**a**) Sample 1 and (**b**) Sample 2 over time and (**c**) the comparison of the variations in mechanical and hydraulic apertures
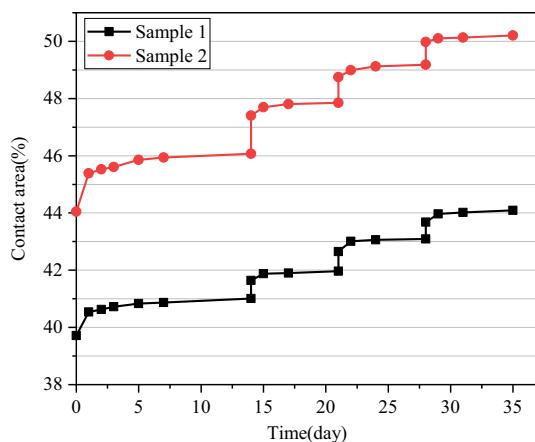

Fig. 10 The time-dependent variation in contact area of two samples during the loading

5 Discussion

5.1 Time-Dependent Behavior of the Fracture Permeability

5.1.1 Creep-Induced Variation in Fracture Permeability and Aperture

The time-dependent behavior of the fracture permeability and aperture observed in many experiments can be attributed to various mechanisms, including mechanical creep, pressure solution, stress corrosion, dissolution/precipitation, and fines migration (Bandara et al. 2021; Chen et al. 2022; Guo et al. 2018; Kamali-Asl et al. 2018; Polak et al. 2003; Yasuhara and Elsworth 2008). Considering single-phase gas flow in our experiment, the dominant mechanism is likely mechanical creep or fines migration. Fines migration is a process in which crushed fine grains migrate with the gas flow to fill or block small

apertures and thus reduce permeability. However, we did not observe particles on the fracture surfaces after the experiment, which indicates that particle clogging is not the primary mechanism but mechanical creep compaction. Creep refers to the deformation process of the rock with time under a constant normal stress (Heap et al. 2009). As shown in Figs. 7 and 9, the time-dependent variation in k_{app} and aperture under each confining stress can be roughly divided into two stages. Such behavior is analogous to the primary and secondary creep stages observed in deformation experiments (Chang and Zoback 2009; Hamza and Stace 2018; Rassouli and Zoback 2018). This suggests that the time-dependent reductions in fracture permeability and aperture are closely related to the creep deformation process of the fracture. Creep-induced fracture deformation changes the geometry of the contacting asperities and void spaces adjacent to these contacting asperities, as well as the contact area of the fracture surface, resulting in the alteration of the hydraulic properties of the fracture (Pyrak-Nolte and Morris 2000). In our experiments, after the application of confining stress (10 MPa), most of the asperities of the two fracture surfaces come into contact, inducing high-stress concentrations (Cheng et al. 2021). Due to the contact, sliding, rearrangement, and crushing of asperities under a constant confining stress, the fracture apertures are squeezed, and the resulting contact areas are gradually expanded, causing a notable reduction in gas flow pathways and an increase in flow tortuosity, thereby leading to a significant decline in gas permeability. As the confining stress increases to a further stage, more asperities come into contact, and the contact area further increases, further reducing the fracture aperture and permeability.

Our experimental results show that the permeability and the associated aperture and contact area change mainly in the elastic deformation stage and the first stage of time-dependent deformation (i.e., the decelerating decline stage). Over time, the two fracture surfaces come closer to each

other, contact occurs at the high asperities, small apertures preferentially close and large apertures remain open. Meanwhile, some isolated apertures are created due to the asperities contact and heterogeneous fracture structures. The gas flow paths are basically determined at the end of this period. As time goes on, subsequent fracture deformation depends almost entirely on the deformability of contacted asperities (Bandis et al. 1983). Creep-induced fracture closure gradually stabilizes in the steady decline stage, where the slight compression of large apertures and the closure of isolated apertures mainly occur, so that the preferential flow paths no longer change, and only minor reductions in fracture permeability and hydraulic aperture are observed. The mechanical aperture changes are always greater than the hydraulic aperture changes because some isolated apertures gradually close during the elastic and creep deformation, and the closure of these isolated apertures has almost no impact on the seepage capacity of the fracture, thus not affecting the change in permeability and hydraulic aperture.

During the loading process, more asperities will come into contact at higher confining stress. Deformation of these contacted asperities is the main source of creep, so the cumulative creep-induced k_{app} reduction increases with confining stress (Fig. 7d). This experimental observation suggests that the time-dependent creep deformation is expected to exert significant effects on the permeability at high formation stresses. Even at the confining stress of 10 MPa in our experiments, a comparison of k_{app} on the first and last day revealed almost a twofold overestimation of permeability if creep effects are not considered. Similar observations have been made by other scholars. Chhatre et al. (2014) stated that the initial permeability of the intact Eagle Ford shale is approximately four times the steady permeability at 2500 psi confining stress due to the creep effect. Bandara et al. (2021) found that for propped sandstone fractures, creep-induced permeability was overestimated by a factor of 1.2–13 under 20 MPa confining stress. If a higher confining stress is applied to our samples in the first loading stage, we may see more pronounced time-dependent variations in

fracture permeability. Therefore, it is important to consider the time-dependent behavior of fracture permeability in numerical simulations or reservoir engineering calculations of underground projects. In addition, Figs. 7 and 8 show an irreversible reduction in permeability and slight permeability recovery in the unloading process. This is attributed to the fact that the creep compaction of shale fractures is nearly irrecoverable deformation and characterized as a combination of viscoelastic and viscoplastic behavior (Chang and Zoback 2009; Sone and Zoback 2014). The rearrangement and crushing of asperities in fracture surfaces are irreversible, and the reduced apertures are difficult to recover. The variations in fracture permeability during unloading are insignificant under each confining stress, and creep plays little role in this process.

5.1.2 Time-Dependent Variation in Gas Slippage

The experimental results in Table 5 show that the gas permeabilities of the two samples decrease with increasing gas pressure under all confining stresses. k_{app} declines up to 1.4 times as the gas pressure increases from 0.6 to 1.3 MPa in Sample 1, and it declines up to 1.2 times as the gas pressure increases from 0.6 to 1.5 MPa in Sample 2. This gas pressure-dependent behavior of gas permeability is due to the gas slippage effect in the fracture (Klinkenberg 1941). According to the theory of Klinkenberg (1941), the mean free path of gas molecules varies with gas pressure, and when the mean free flow path of the methane molecules approaches the aperture size, the collisions between gas molecules and fracture walls become dominant, inducing additional gas fluxes near the fracture surfaces. Similar phenomena have been reported by many scholars in fractures of different rock types, including siltstone (Wanniarachchi et al. 2018), sandstone (Bandara et al. 2021), and shale samples (Cheng and Yu 2022). Figure 11 indicates that k_{app} is inversely proportional to the average gas pressure, and the

Fig. 11 Relationship between the apparent gas permeability and reciprocal of the gas pressure
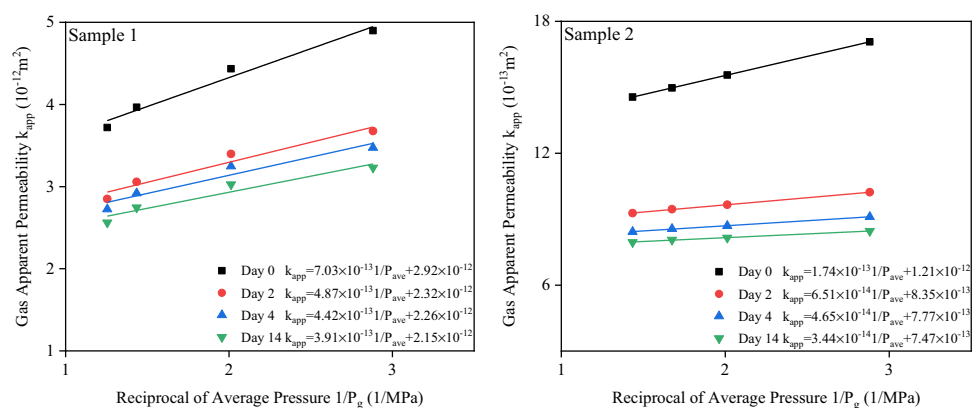
linear relationship can be expressed as follows (Klinkenberg 1941):

$$k_{\mathrm{app}} = k_{\mathrm{in}}\left(1 + \frac{b}{P_g}\right), \tag{15}$$

where k_{in} is the intrinsic permeability; P_g is the average gas pressure, which can be calculated as $P_g = (P_1 + P_2)/2$; and b is the slippage factor, which indicates the influence degree of gas slippage on the total gas flow. The values of k_{in} and b under different confining stresses are determined by fitting the experimental results based on Eq. (15). The results show that the contribution of slip flow can reach 40% in the experimental ranges of gas pressure.

As shown in Fig. 11, at a constant 10 MPa confining stress, the slope of both plots decreases with time, indicating that the gas slippage effect weakens over time. We then calculated the time-dependent variation in slippage factor b using data collected under 10 MPa confining stress as an example. Figure 12 shows that b presents a gradual

Fig. 12 Relationship between the slippage factor and time at a confining stress of 10 MPa

decline with time. Fitting the experimental data indicates that b decays as a power function with time, which can be expressed as follows:

$$b = b_0 - m \times (1 - n^t), \tag{16}$$

where b_0 is the initial slippage factor at 0 days and m and n are fitting parameters. Equation (16) is also applicable to other confining stresses, and the fitting parameters are listed in Table 6.

Note that the trend of b can be divided into two stages, which is consistent with the variation in permeability, with a high decrease rate in the primary stage and then a slight decrease rate during the secondary stage. Theoretically, the slippage factor can be expressed as (Cheng and Yu 2022; Zaouter et al. 2018):

$$b = \frac{6K_B T\zeta}{\sqrt{2}\pi\delta^2 e}. \tag{17}$$

Equation (17) suggests that the slippage factor is inversely proportional to the fracture aperture and that the gas slippage effect is significant at small apertures. Some scholars have stated that b increases with effective stress because the increasing stress constricts pore channels (Chen et al. 2021; Meng et al. 2021). One might expect that the fracture void space would be compressed under a constant confining stress and the gas slippage would be enhanced with time. However, the opposite phenomenon was observed in our experiments. As mentioned in Sect. 5.1.1, small apertures gradually close due to creep in the primary stage, while most of the large apertures remain open. The decreasing number of apertures most responsible for the gas slippage leads to the reduction in b over time. During the secondary stage, the aperture distribution is stable, and fluid pathways are formed, so the gas slippage barely changes.

Table 6 Parameters of the permeability model at different confining stresses

| Sample	P_c (MPa)	E_2 (GPa)	η_1 (GPa h)	η_2 (GPa·h)	B (MPa^{-1})	D	m (MPa)	n	b_o (MPa)
1	10	0.098	51.941	1.078	5.560E-3	0.170	0.054	0.982	0.241
	15	0.681	223.926	6.724	7.107E-4	0.219	0.034	0.979	0.269
	20	1.156	238.115	14.820	3.090E-4	0.313	0.042	0.941	0.146
	25	1.273	353.631	16.320	2.388E-4	0.322	0.038	0.962	0.068
2	10	0.063	31.030	0.403	1.001E-2	0.141	0.093	0.974	0.144
	15	0.555	172.163	6.090	8.100E-4	0.237	0.013	0.964	0.050
	20	0.722	303.823	7.510	6.965E-4	0.201	0.016	0.981	0.084
	25	1.168	367.224	25.978	1.972E-4	0.375	0.021	0.958	0.067

5.1.3 Factors Influence the Time-Dependent Fracture Permeability

The experimental results show that although the permeability presents a similar variation trend at each confining stress stage, the magnitude of variation gradually decreases with increasing stress. This behavior probably results from the change in fracture normal stiffness (Bandis et al. 1983; Cammarata et al. 2006; Li et al. 2021; Liu et al. 2012). Figure 13a shows the fracture stiffness calculated from the confining stress and aperture variation of the two fractured samples during the loading phase. The fracture normal stiffness is related to the mechanical properties of the contacted asperities and depends mainly on the amount and distribution of the fracture contact area (Brown and Scholz 1985; Cheng and Milsch 2021; Pyrak-Nolte and Morris 2000). To investigate the interrelationship between fracture stiffness and time-dependent permeability, the variation in permeability (percentage) during each confining stress stage is displayed in Fig. 13b. When the sample is first subjected to confining stress (10 MPa), the contact area and fracture stiffness are low, and the fracture is easily compressed, resulting in a major time-dependent variation in fracture permeability. As the confining stress rises, more contact asperities are formed. The increasing contact area can withstand higher stresses, and the fracture stiffness gradually increases (Zhao et al. 2017). Only slight fracture compaction and permeability reduction occur at higher confining stresses. Therefore, as shown in Fig. 13, the noteworthy difference in the magnitude of reduction in permeability at the first two confining stress levels (10 and 15 MPa) is ascribed to the dramatic increase in fracture stiffness. Under the subsequent confining stresses (15, 20, and 25 MPa), the difference in the time-dependent permeability reduction between each stage is not significant, but it still decreases with increasing fracture stiffness. This may be because the fracture stiffness is already large and the deformability of the fracture is very poor. The continuous increase in fracture stiffness does not have a noticeable effect on fracture deformation (i.e., permeability reduction) as it did initially. Moreover, combining Figs. 8 and 13, it can be inferred that in our multilevel confining stress experiments, the fracture stiffness increases after each stress level, which has a greater impact on the instantaneous reduction in fracture permeability than the time-dependent reduction in permeability. The decline in Δk_i is apparently greater than that in Δk_c, and thus the ratio of Δk_c to Δk_i increases during loading. This suggests that the time-dependent creep compaction exhibits an increasingly important role in dominating the fracture closure and transport capacity with increasing confining stress. Chang and Zoback (2009) also observed the stiffening effect in Gulf of Mexico shale at higher stresses. They found that the creep strain was larger than the elastic strain when the stress increased above 20 MPa.

Figure 13b reveals a different degree of the time-dependent reduction in permeability for the two samples under a constant P_c, which may be closely related to the fracture surface morphology, aperture distribution, mechanical properties, and mineral composition (An et al. 2021; Kamali-Asl et al. 2018; Zhang et al. 2021). The 3-D surface topography and the aperture measurements show that Sample 2 is rougher than Sample 1, and the average aperture of Sample 1 is approximately four times larger than that of Sample 2, which corresponds to the lower fracture permeability of Sample 2 than Sample 1. As shown in Fig. 6, the aperture distribution range of Sample 1 is wider than that of Sample 2. Considering that the narrow apertures will be closed preferentially under stress, more void spaces remain in Sample 1, while more asperities on the fracture surfaces in Sample 2 will be in contact. This could explain why the permeability of Sample 2, which has a higher fracture stiffness, shows a greater reduction magnitude than that of Sample 1 at a 10 MPa confining stress and why the permeability of Sample 1 is consistently higher than that of Sample 2. If so, Sample 2 will have more deformed asperities than Sample 1, thereby resulting in a larger irreversible amount of gas permeability in Sample 2. At the following higher confining stresses, the reduction in permeability of Sample 1 is slightly larger than that of Sample 2, which is associated with the difference in fracture stiffness between the two samples. Fracture stiffness is directly related to elastic modulus, and Sample

Fig. 13 **a** The variation in fracture stiffness with confining stress and **b** the magnitude of the time-dependent reduction in permeability at each confining stress
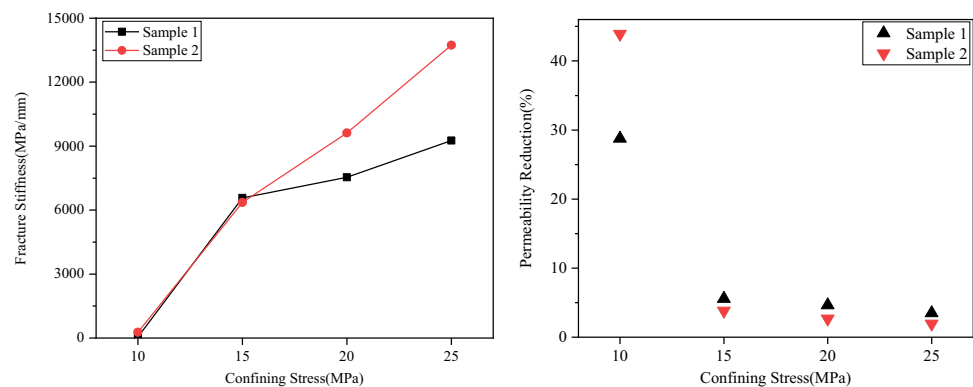
1 with less fracture stiffness means it is easier to deform than Sample 2. In addition, previous studies on fractures indicate that the fracture stiffness is proportional to the JRC value (fracture geometry) and contact area (Bandis et al. 1983; Pyrak-Nolte and Morris 2000), and fracture stiffness is implicitly related to the rock mineral composition through the mechanical properties of contact asperities. The presence of soft material such as clay and total organic carbon (TOC) in fractured rocks decreases the fracture stiffness, and the amount of creep deformation is correlated to the clay and TOC contents (Rassouli and Zoback 2018; Sone and Zoback 2013). Considering that the clay and TOC contents of Sample 1 are higher than those of Sample 2 and the elastic modulus, JRC value, and contact area of Sample 1 are smaller than those of Sample 2, Sample 1 thus exhibits more time-dependent reduction in permeability than Sample 2. In summary, the size and spatial distribution of the apertures mainly control the time-dependent permeability variation during the first loading stage, and the dominant influence factor of time-dependent permeability converts to fracture stiffness at higher confining stress levels.

5.2 Time-Dependent Gas Permeability Model of the Fracture

A mathematical model to quantitatively describe the time-dependent behavior of the gas permeability in a fracture under formation stress is critical for predicting the long-term response of fractures associated with geotechnical performance and engineering design under reservoir conditions (An et al. 2021; Bandara et al. 2021; Kamali-Asl et al. 2020). In this study, we propose a gas permeability model that considers the coupled effects of gas slippage and long-term creep of the fracture.

Burgers and Power-law models have been widely used to model and predict the creep behavior of rock (Hamza and Stace 2018; Kaiser and Morgenstern 1982; Kamali-Asl et al. 2021; Sone and Zoback 2014). The Burgers model, which can describe elastic, primary, and steady-state creep deformation, is composed of a Kelvin model (a spring and a dashpot connected in series) and a Maxwell model (a spring and a dashpot connected in parallel) in series (Nomikos et al. 2011; Parsons and Hedley 1966), and it is expressed as follows:

$$\varepsilon = \sigma\left[\frac{1}{E_1} + \frac{t}{\eta_1} + \frac{1}{E_2}\left(1 - e^{-\frac{E_2 t}{\eta_2}}\right)\right], \tag{18}$$

where ε denotes strain; σ represents the applied stress on the fracture; E_1 and η_1 are the spring modulus and dashpot viscosity for the Maxwell unit; and E_2 and η_2 are the spring modulus and dashpot viscosity for the Kelvin unit. The Power-law model can fit the creep data well, which is

simpler and safer when extrapolated (Rassouli and Zoback 2018; Trzeciak et al. 2018). It can be expressed as (Sone and Zoback 2014):

$$\varepsilon = \frac{\sigma}{E} + \sigma Bt^D, \tag{19}$$

where E is Young's modulus and B and D are empirical parameters.

In a fracture, ε can be quantified by the aperture variation, defined as the ratio of the aperture variation (Δe) to the initial aperture (e_0). The first term in both equations represents the elastic strain, and only the creep strain induced by the confining stress P_c is considered in this study. Equations (18) and (19) are thus transformed into the following form:

$$\frac{\Delta e}{e_0} = P_c\left[\frac{t}{\eta_1} + \frac{1}{E_2}\left(1 - e^{-\frac{E_2 t}{\eta_2}}\right)\right], \tag{20}$$

$$\frac{\Delta e}{e_0} = P_c Bt^D. \tag{21}$$

According to the cubic law, the fracture permeability (k) is correlated to the aperture variation Δe, and thus k can be rewritten as follows:

$$k = k_0(1 - \frac{\Delta e}{e_0})^2, \tag{22}$$

where k_0 is the initial permeability value. According to Eqs. (20)–(22), the time-dependent permeability of the fracture can be determined as follows:

$$k = k_0\left[1 - P_c\left[\frac{t}{\eta_1} + \frac{1}{E_2}\left(1 - e^{-\frac{E_2 t}{\eta_2}}\right)\right]\right]^2, \tag{23}$$

$$k = k_0\left(1 - P_c Bt^D\right)^2. \tag{24}$$

Notably, k in Eqs. (23) and (24) is the intrinsic permeability reflecting the intrinsic properties of the rock but not the apparent gas permeability (k_{app}). Equations (23) and (24) cannot be directly used to model our experimental results due to the gas slippage effect.

Combining Eqs. (15) and (16), Eqs. (23) and (24) can be transformed as follows:

$$k_{app} = k_{app0}\left[1 - P_c\left[\frac{t}{\eta_1} + \frac{1}{E_2}\left(1 - e^{-\frac{E_2 t}{\eta_2}}\right)\right]\right]^2\left[1 - \frac{m(1 - n^t)}{P_g + b_0}\right], \tag{25}$$

$$k_{app} = k_{app0}\left(1 - P_c Bt^D\right)^2\left[1 - \frac{m(1 - n^t)}{P_g + b_0}\right]. \tag{26}$$

We then verified the gas permeability models based on the experimental results. The experimental data (data for 7
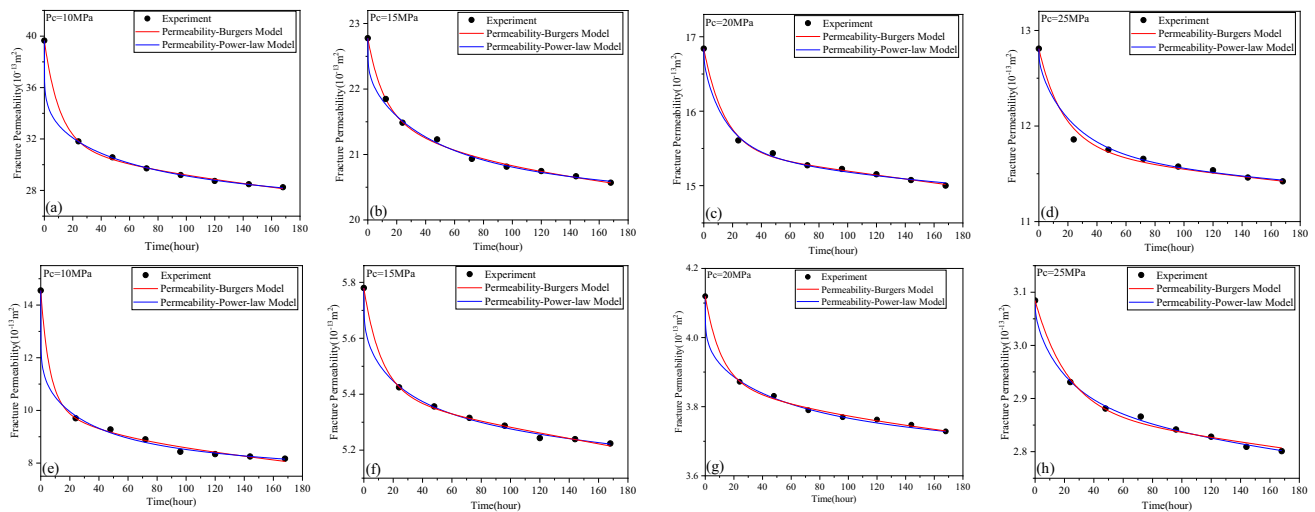
Fig. 14 Comparison between experimental data and two permeability models at each confining stress

days within each confining stress level) are used to fit the two models and obtain the best-fit model parameters, including η_1, E_2, η_2, B, and D. Figure 14 shows that both Eqs. (25) and (26) can match the experimental data well, indicating that the two models are suitable for describing the time-dependent variation in fracture permeability during flow-through experiments with good accuracy ($R^2 = 0.97$–0.99). The associated parameters are determined at confining stresses of 10, 15, 20, and 25 MPa and displayed in Table 6. The parameters E_2 and η_2 reflect the property of primary creep stage and the parameter η_1 exhibits the property of secondary creep stage (Hamza and Stace 2018). The lower parameter values mean a greater decrease in the fracture permeability during the corresponding creep stage. These three parameters are related to the fracture stiffness and contact area. The fracture stiffness of the sample is very low when it is first stressed. With increasing confining stress P_c and loading time, the contact area between the two fracture surfaces also increases, increasing the fracture stiffness. The lower fracture stiffness suggests that the fractured sample is prone to exert deformation, thereby resulting in much more permeability reduction under P_c of 10 MPa compared to that under the other higher stresses, which corresponds to the smallest values of these three parameters. An increase in E_2 and η_2 with increasing P_c indicates that the duration and magnitude of permeability reduction in the primary stage diminish at higher P_c. The η_1 increases with P_c means that the decline rate of permeability in the steady decline stage decreases. These behaviors are consistent with our experimental observations and can be attributed to the fact that increasing fracture stiffness with increasing P_c and loading time results in a weakening of the fracture deformation capacity. In the Power-law model, B is roughly inversely proportional to the elastic Young's modulus. Parameter D determines the

relative contribution of the time-dependent strain to the total strain (Sone and Zoback 2014). The decrease of B value with increasing P_c (especially 10 to 15 MPa) can be attributed to the increasing fracture stiffness after subjected each stress step. Larger values of D at higher P_c indicate that time-dependent permeability variations become more important. Since the increase in the fracture stiffness affects Δk_i more than Δk_c, the ratio of Δk_c to Δk_i rises progressively (Fig. 8), which is consistent with the increase in D value.

The two permeability models are valid in the experimental time (seven days), but the capability of the two models to predict variations in fracture permeability in long-term subsurface engineering deserves further examination. We used the model parameters obtained by fitting the 7 days of data (parameters in Table 6) to calculate the permeability changes within 14 days under 10 MPa confining stress and compared them with the experimental values to verify the practicability of the model. Figure 15a shows that the theoretical permeability calculated by the Burgers-permeability model deviates from the experimental data with time, while the Power-law-permeability model can better predict the trend of the decrease in permeability. In addition, to further evaluate the usefulness of the Power-law-permeability model, it is examined whether this model can successfully fit experimental results from other sources. Bandara et al. (2021) measured fracture gas permeability for saturated siltstone, and the creep-induced permeability variations at 20 MPa confining stress were observed. The experimental data are extracted and plotted in Fig. 15b, where the measurement time is 144 h. The gas slippage effect in those samples is considered and calculated from the flow-through test data. In Fig. 15b, the permeability model is well matched with the experimental data. Therefore, the Power-law-permeability model is effective, and by providing appropriate

Fig. 15 **a** Comparison of the capacity of two models to predict permeability variation and **b** verification of the applicability of the Power-law-permeability model by other published results (Bandara et al. 2021)
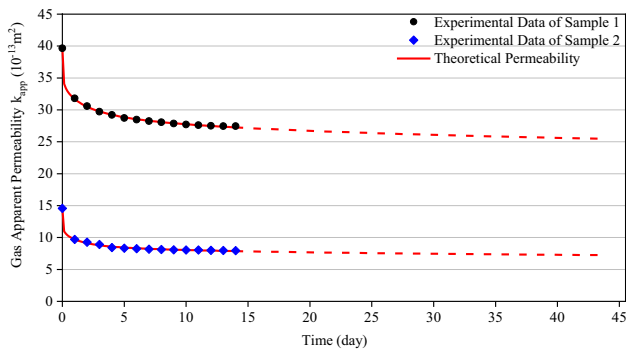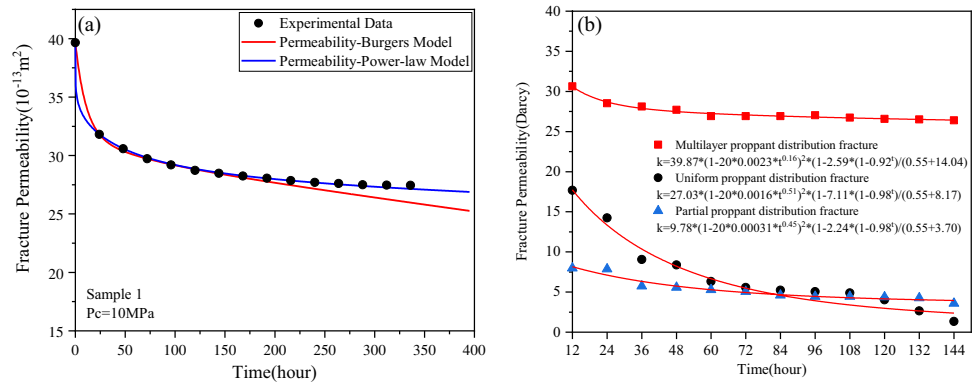

Fig. 16 The predicted permeability reduction over the next 30 days using the time-dependent permeability model at a confining stress of 10 MPa

rock parameters and associated coefficients, it can be used to predict the time-dependent permeability variations in large-scale underground projects.

As shown in Fig. 16, the permeability variations over the next 30 days are predicted by the permeability model. Although the permeability changes slowly, further permeability reductions of 6.6% and 8.0% are produced in Samples 1 and 2, which account for 15.7% and 9.8% of the permeability decline in the first 7 days, respectively. This implies that most of the time-dependent permeability reduction in the fractured sample under constant stress occurs over the first week. Based on the trends of permeability variation predicted by the model, a certain amount of permeability loss may be expected during the long-term compaction phase of subsurface fractures over decades or centuries. This time-dependent compaction is likely to be an action mechanism that induces the self-sealing of the fracture. However, fractures are difficult to close completely within a short time due to the interaction of the asperities on the two opposing fracture surfaces (Zhao et al. 2017; Zhou et al. 2019). Under long-term formation stress, the rock fractures gradually stiffen so

that the permeability reductions in the later phases are extremely low. The validity of this permeability model may need to be further verified by actual data on a larger time scale.

5.3 Implications

Fracture permeability measurements of shale cores are routinely conducted in the laboratory at approximate in situ stress conditions, and the experimental conclusions can be extended to the field scale for efficient implementation of underground engineering. The study of creep-induced time-dependent permeability evolution in fractured shale is important but challenging because it takes a long time. Our experiments show that fracture permeability would be significantly overestimated if the creep effect is not taken into account. Gas slippage, as a gas-specific property that influences gas permeability (Chen et al. 2020; Cheng and Yu 2022), is also affected by creep, exhibiting a power function decay with time. The rate of permeability change decreases continuously and then stabilizes over time under the constant confining stress. After approximately five days, the permeability gradually enters a quasi-stable stage. Therefore, to accurately measure rock permeability, one can either apply a certain confining stress to the rock sample in the core holder for at least a week before permeability measurements or successively measure the permeability until it reaches a quasi-stable value. Using the proposed permeability model to calculate the time-dependent variation caused by creep is also a way to roughly eliminate measurement errors and improve accuracy. Note that our permeability model is relatively simple, and determining the right model parameters is necessary. More data from flow-through experiments and deformation experiments are required to strengthen the model practicability.

Shale-gas/oil development relies on multistage fracturing and horizontal drilling technology (An et al. 2021; Zhou et al. 2019). These advanced engineering activities create

numerous fractures. Correct evaluation of shale fracture permeability is crucial to understanding and predicting reservoir production performance. Our experimental results indicate that creep compaction greatly reduces the transport capacity of shale fractures during the first loading stage, while this effect is weakened at higher confining stresses due to the increase in fracture stiffness. This means that newly generated self-propping fractures will exhibit a certain time-dependent permeability reduction under formation stress, and as the effective stress rises (for example, during resource depletion), those fractures will only be slightly compacted and may persist for a long time. Shales are also considered as caprocks or host rocks for CO_2 geological sequestration and radioactive waste geological disposal (Cheng and Yu 2019; Tsang et al. 2012). Fractures, as the most probable leakage pathways, determine the success or failure of these underground projects (Zaouter et al. 2018). An effective prediction of the seepage characteristics of subsurface fluids during the disposal period is necessary for the long-term safety of geological disposal repositories. Our data show that the fracture permeability changes slightly at the end of each confining stress stage. Dry fractures are difficult to close completely under creep. Previous studies have demonstrated that moisture can promote mechanical creep, clay swelling, or even complete self-sealing (Sone and Zoback 2014; Wang et al. 2022; Wenning et al. 2021; Zhang and Talandier 2022). Therefore, introducing some aqueous fluids to accelerate fracture creep (i.e., enhance the time-dependent reduction of fracture permeability) is required to prevent shallow groundwater contamination caused by leakage of greenhouse gases and radioactive waste. Compared with dry fractures, the evolution of the seepage characteristics over time of water-saturated fractures under hydro-mechanical coupling effect is more complex and thus needs to be further investigated and elucidated in future work.

6 Conclusions

A series of gas permeability measurements and associated aperture calculations were conducted on shale microfractures under multilevel confining stresses to experimentally investigate the time-dependent behavior of the gas permeability and underlying mechanisms. The following conclusions were reached.

The observed permeability reduction of up to 3.8–5.2 times during confining stress loading from 10 to 25 MPa is a result of the elastic deformation and creep of the fracture. The gas permeability and aperture of the fracture significantly decrease with time due to creep at a constant confining stress, with a rapid and decelerating decline stage

and then a slow and steady decline stage. Neglecting creep effects can lead to an overestimation of fracture permeability by at least two times under 10 MPa confining stress. Considering the time-dependent creep behavior of fractures is essential in calculating fracture permeability for numerical simulations or reservoir engineering calculations of underground projects.

Increasing confining stress results in a decrease in the effective aperture and an increase in the contact area of the fracture, thereby further decreasing the gas permeability, but the permeability reductions caused by both elastic deformation (Δk_i) and creep (Δk_c) are weakened. This behavior is related to the increase in fracture stiffness. The considerable decline in the magnitude of permeability reduction is due to the dramatically increase in fracture stiffness. The increase in fracture stiffness with confining stress has a greater effect on Δk_i than on Δk_c; thus, the ratio of Δk_c to Δk_i also increases with confining stress. During the unloading phase, permanent permeability loss and limited permeability recovery over time are observed, indicating that the creep-induced permeability reduction is an irrecoverable process. Our results also show that two fractured samples exhibit different time-dependent permeability reductions, which are attributed to differences in aperture distributions and fracture stiffness.

The dependence of permeability on gas pressure indicates the presence of the gas slippage phenomenon in the fractures. The contribution of slip flow can be up to 40%, even in a relatively small gas pressure range. Under a constant confining stress, gas slippage manifests a power function decay over time with the change of aperture distribution caused by creep. Considering the coupling effect of creep compaction and gas slippage, the time-dependent gas permeability model is developed and verified by experimental data. Subsequently, the permeability reductions over the next 30 days are predicted by this model. The predicted results suggest that the gas permeability of the two samples decreases further during this period, but to a small extent.

Author Contributions NZ: conceptualization, methodology, experiment, data processing and analysis, writing—original draft. PC: methodology, investigation, writing—review and editing. QY: conceptualization, supervision, review and editing, project administration, funding acquisition, resources.

Data Availability Detailed experimental data used in this study will be provided upon request.

Declarations

Conflict of Interest The authors declare that they have no known competing financial interests or personal relationships that could have appeared to influence the work reported in this paper.

References

An C, Killough J, Xia XY (2021) Investigating the effects of stress creep and effective stress coefficient on stress-dependent permeability measurements of shale rock. J Petrol Sci Eng 198:108155. https://doi.org/10.1016/j.petrol.2020.108155

Bachu S (2000) Sequestration of CO2 in geological media: criteria and approach for site selection in response to climate change. Energy Convers Manage 41(9):953–970. https://doi.org/10.1016/S0196-8904(99)00149-1

Bandara KMAS, Ranjith PG, Haque A, Wanniarachchi WAM, Zheng W, Rathnaweera TD (2021) An experimental investigation of the effect of long-term, time-dependent proppant embedment on fracture permeability and fracture aperture reduction. Int J Rock Mech Min Sci 144(B7):104813. https://doi.org/10.1016/j.ijrmms.2021.104813

Bandis SC, Lumsden AC, Barton NR (1983) Fundamentals of rock joint deformation. Int J Rock Mech Min Sci Geomech Abstr 20(6):249–268. https://doi.org/10.1016/0148-9062(83)90595-8

Berkowitz B (2002) Characterizing flow and transport in fractured geological media: a review. Adv Water Resour 25(8–12):861–884. https://doi.org/10.1016/S0309-1708(02)00042-8

Brown SR, Scholz CH (1985) Closure of random elastic surfaces in contact. J Geophys Res Solid Earth 90(B7):5531–5545. https://doi.org/10.1029/JB090iB07p05531

Busch A, Alles S, Gensterblum Y, Prinz D, Dewhurst DN, Raven MD, Stanjek H, Krooss BM (2008) Carbon dioxide storage potential of shales. Int J Greenhouse Gas Control 2(3):297–308. https://doi.org/10.1016/j.ijggc.2008.03.003

Cammarata G, Fidelibus C, Cravero M, Barla G (2006) The hydromechanically coupled response of rock fractures. Rock Mech Rock Eng 40(1):41–61. https://doi.org/10.1007/s00603-006-0081-z

Cardona A, Finkbeiner T, Santamarina JC (2021) Natural rock fractures: from aperture to fluid flow. Rock Mech Rock Eng 54(11):5827–5844. https://doi.org/10.1007/s00603-021-02565-1

Chang CD, Zoback MD (2009) Viscous creep in room-dried unconsolidated Gulf of Mexico shale (I): experimental results. J Petrol Sci Eng 69(3–4):239–246. https://doi.org/10.1016/j.petrol.2009.08.018

Chen Y-F, Zhou J-Q, Hu S-H, Hu R, Zhou C-B (2015) Evaluation of Forchheimer equation coefficients for non-Darcy flow in deformable rough-walled fractures. J Hydrol 529:993–1006. https://doi.org/10.1016/j.jhydrol.2015.09.021

Chen Y, Jiang C, Leung JY, Wojtanowicz AK, Zhang D (2020) Gas slippage in anisotropically-stressed shale: an experimental study. J Petrol Sci Eng 195:107620. https://doi.org/10.1016/j.petrol.2020.107620

Chen Y, Jiang C, Leung JY, Wojtanowicz AK, Zhang D, Zhong C (2021) Second-order correction of Klinkenberg equation and its experimental verification on gas shale with respect to anisotropic stress. J Nat Gas Sci Eng 89:103880. https://doi.org/10.1016/j.jngse.2021.103880

Chen X, Xie SY, Zhang W, Armand G, Shao JF (2022) Creep deformation and gas permeability in fractured claystone under various stress states. Rock Mech Rock Eng 55(4):1843–1853. https://doi.org/10.1007/s00603-022-02774-2

Cheng C, Milsch H (2021) Hydromechanical investigations on the self-propping potential of fractures in tight sandstones. Rock Mech Rock Eng 54(10):5407–5432. https://doi.org/10.1007/s00603-021-02500-4

Cheng PJ, Yu QC (2019) Experimental study on the relationship between the matric potential and methane breakthrough pressure of partially water-saturated shale fractures. J Hydrol 578:124044. https://doi.org/10.1016/j.jhydrol.2019.124044

Cheng PJ, Yu QC (2022) Gas slippage in microscale fractures of partially saturated shale of different matric potentials. SPE J 27(5):3020–3034. https://doi.org/10.2118/209803-pa

Cheng CJ, Herrmann J, Wagner B, Leiss B, Stammeier JA, Rybacki E, Milsch H (2021) Long-term evolution of fracture permeability in slate: an experimental study with implications for enhanced geothermal systems (EGS). Geosciences 11(11):443. https://doi.org/10.3390/geosciences11110443

Chhatre SS, Sinha S, Braun EM, Esch WL, Determan MD, Passey QR, Leonardi SA, Zirkle TE, Wood AC, Boros JA, Kudva RA (2014) Effect of Stress, Creep, and Fluid Type on Steady State Permeability Measurements in Tight Liquid Unconventional Reservoirs. In:Proceedings of the 2nd Unconventional Resources Technology Conference

Cho Y, Apaydin OG, Ozkan E (2013) Pressure-dependent natural-fracture permeability in shale and its effect on shale-gas well production. SPE Reservoir Eval Eng 16(2):216–228. https://doi.org/10.2118/159801-Pa

Danesh NN, Chen Z, Aminossadati SM, Kizil MS, Pan Z, Connell LD (2016) Impact of creep on the evolution of coal permeability and gas drainage performance. J Nat Gas Sci Eng 33:469–482. https://doi.org/10.1016/j.jngse.2016.05.033

Deng J, Zhu WY, Ma Q (2014) A new seepage model for shale gas reservoir and productivity analysis of fractured well. Fuel 124:232–240. https://doi.org/10.1016/j.fuel.2014.02.001

Deng Q, Blöcher G, Cacace M, Schmittbuhl J (2021) Hydraulic diffusivity of a partially open rough fracture. Rock Mech Rock Eng 54(10):5493–5515. https://doi.org/10.1007/s00603-021-02629-2

Elkhoury JE, Detwiler RL, Ameli P (2015) Can a fractured caprock self-heal? Earth Planet Sci Lett 417:99–106. https://doi.org/10.1016/j.epsl.2015.02.010

Gao J, Yu Q, Lu X (2017) Apparent permeability and gas flow behavior in carboniferous shale from the Qaidam Basin, China: an experimental study. Transp Porous Media 116(2):585–611. https://doi.org/10.1007/s11242-016-0791-y

Guo ZH, Vu PNH, Hussain F (2018) A laboratory study of the effect of creep and fines migration on coal permeability during single-phase flow. Int J Coal Geol 200:61–76. https://doi.org/10.1016/j.coal.2018.10.009

Hamza O, Stace R (2018) Creep properties of intact and fractured muddy siltstone. Int J Rock Mech Min Sci 106:109–116. https://doi.org/10.1016/j.ijrmms.2018.03.006

Heap MJ, Baud P, Meredith PG, Bell AF, Main IG (2009) Time-dependent brittle creep in Darley Dale sandstone. J Geophys Res. https://doi.org/10.1029/2008jb006212

Isaka BLA, Ranjith PG, Wanniarachchi WAM, Rathnaweera TD (2020) Investigation of the aperture-dependent flow characteristics of a supercritical carbon dioxide-induced fracture under high-temperature and high-pressure conditions: a numerical study. Eng Geol 277:105789. https://doi.org/10.1016/j.enggeo.2020.105789

Kaiser PK, Morgenstern NR (1982) Time-independent and time-dependent deformation of small tunnels. 3. Pre-failure behavior. Int J Rock Mech Min Sci 19(6):307–324. https://doi.org/10.1016/0148-9062(82)91366-3

Kamali-Asl A, Ghazanfari E, Perdrial N, Bredice N (2018) Experimental study of fracture response in granite specimens subjected to hydrothermal conditions relevant for enhanced geothermal

systems. Geothermics 72:205–224. https://doi.org/10.1016/j.geothermics.2017.11.014

Kamali-Asl A, Ghazanfari E, Perdrial N, Cladouhos T (2020) Effects of injection fluid type on pressure-dependent permeability evolution of fractured rocks in geothermal reservoirs: an experimental chemo-mechanical study. Geothermics 87:101832. https://doi.org/10.1016/j.geothermics.2020.101832

Kamali-Asl A, Kc B, Ghazanfari E, Falcon-Suarez IH (2021) Alteration of ultrasonic signatures by stress-induced changes in hydromechanical properties of fractured rocks. Int J Rock Mech Min Sci 142:104705. https://doi.org/10.1016/j.ijrmms.2021.104705

Klinkenberg LJ (1941) The permeability of porous media to liquids and gases. Drill Prod Pract 1941:200–213

Li J, Chen Z, Wu K, Li R, Xu J, Liu Q, Qu S, Li X (2018) Effect of water saturation on gas slippage in tight rocks. Fuel 225:519–532. https://doi.org/10.1016/j.fuel.2018.03.186

Li B, Cui X, Zou L, Cvetkovic V (2021) On the relationship between normal stiffness and permeability of rock fractures. Geophys Res Lett 48(20):e2021GL095593. https://doi.org/10.1029/2021gl095593

Liang ZR, Chen ZX, Rahman SS (2020) Experimental investigation of the primary and secondary creep behaviour of shale gas reservoir rocks from deep sections of the Cooper Basin. J Nat Gas Sci Eng 73:103044. https://doi.org/10.1016/j.jngse.2019.103044

Liu H-H, Wei M-Y, Rutqvist J (2012) Normal-stress dependence of fracture hydraulic properties including two-phase flow properties. Hydrogeol J 21(2):371–382. https://doi.org/10.1007/s10040-012-0915-6

Liu L, Xu WY, Wang HL, Wang W, Wang RB (2016a) Permeability evolution of granite gneiss during triaxial creep tests. Rock Mech Rock Eng 49(9):3455–3462. https://doi.org/10.1007/s00603-016-0999-8

Liu ZB, Shao JF, Liu TG, Xie SY, Conil N (2016b) Gas permeability evolution mechanism during creep of a low permeable claystone. Appl Clay Sci 129:47–53. https://doi.org/10.1016/j.clay.2016.04.021

Matsuki K, Wang EQ, Sakaguchi K, Okumura K (2001) Time-dependent closure of a fracture with rough surfaces under constant normal stress. Int J Rock Mech Min Sci 38(5):607–619. https://doi.org/10.1016/S1365-1609(01)00022-3

Meng Y, Li Z, Lai F (2021) Influence of effective stress on gas slippage effect of different rank coals. Fuel 285:119207. https://doi.org/10.1016/j.fuel.2020.119207

Milne D (1990) Standardized joint descriptions for improved rock classification. In: Rock mechanics contributions and challenges. Proceedings of the 31st U.S. Symposium on Rock Mechanics. Balkema, Rotterdam

Nemoto K, Watanabe N, Hirano N, Tsuchiya N (2009) Direct measurement of contact area and stress dependence of anisotropic flow through rock fracture with heterogeneous aperture distribution. Earth Planet Sci Lett 281(1):81–87. https://doi.org/10.1016/j.epsl.2009.02.005

Nomikos P, Rahmannejad R, Sofianos A (2011) Supported axisymmetric tunnels within linear viscoelastic burgers rocks. Rock Mech Rock Eng 44(5):553–564. https://doi.org/10.1007/s00603-011-0159-0

Parsons RC, Hedley DGF (1966) The analysis of the viscous property of rocks for classification. Int J Rock Mech Min Sci Geomech Abstr 3(4):325–335. https://doi.org/10.1016/0148-9062(66)90012-X

Polak A, Elsworth D, Yasuhara H, Grader AS, Halleck PM (2003) Permeability reduction of a natural fracture under net dissolution by hydrothermal fluids. Geophys Res Lett. https://doi.org/10.1029/2003gl017575

Pyrak-Nolte LJ, Morris JP (2000) Single fractures under normal stress: the relation between fracture specific stiffness and fluid flow. Int

J Rock Mech Min Sci 37(1):245–262. https://doi.org/10.1016/S1365-1609(99)00104-5

Ranjith PG, Darlington W (2007) Nonlinear single-phase flow in real rock joints. Water Resour Res 43(9):W09502. https://doi.org/10.1029/2006wr005457

Rassouli FS, Zoback MD (2018) Comparison of short-term and long-term creep experiments in shales and carbonates from unconventional gas reservoirs. Rock Mech Rock Eng 51(7):1995–2014. https://doi.org/10.1007/s00603-018-1444-y

Rathnaweera TD, Ranjith PG, Perera MSA (2015) Effect of salinity on effective CO2 permeability in reservoir rock determined by pressure transient methods: an experimental study on Hawkesbury sandstone. Rock Mech Rock Eng 48(5):2093–2110. https://doi.org/10.1007/s00603-014-0671-0

Sausse J (2002) Hydromechanical properties and alteration of natural fracture surfaces in the Soultz granite (Bas-Rhin, France). Tectonophysics 348(1–3):169–185. https://doi.org/10.1016/S0040-1951(01)00255-4

Sinha S, Braun EM, Determan MD, Passey QR, Leonardi SA, Boros JA, Wood AC, Zirkle T, Kudva RA (2013) Steady-state permeability measurements on intact shale samples at reservoir conditions—effect of stress, temperature, pressure, and type of gas. In: All Days. Bahrain International Exhibition Centre, Manama, Bahrain

Sone H, Zoback MD (2013) Mechanical properties of shale-gas reservoir rocks—Part 2: ductile creep, brittle strength, and their relation to the elastic modulus. Geophysics 78(5):D390–D399. https://doi.org/10.1190/Geo2013-0051.1

Sone H, Zoback MD (2014) Time-dependent deformation of shale gas reservoir rocks and its long-term effect on the in situ state of stress. Int J Rock Mech Min Sci 69:120–132. https://doi.org/10.1016/j.ijrmms.2014.04.002

Trzeciak M, Sone H, Dabrowski M (2018) Long-term creep tests and viscoelastic constitutive modeling of lower Paleozoic shales from the Baltic Basin, N Poland. Int J Rock Mech Min Sci 112:139–157. https://doi.org/10.1016/j.ijrmms.2018.10.013

Tsang CF, Barnichon JD, Birkholzer J, Li XL, Liu HH, Sillen X (2012) Coupled thermo-hydro-mechanical processes in the near field of a high-level radioactive waste repository in clay formations. Int J Rock Mech Min Sci 49:31–44. https://doi.org/10.1016/j.ijrmms.2011.09.015

Tse R, Cruden D (1979) Estimating joint roughness coefficients. Int J Rock Mech Min Sci Geomech Abstr 16(5):303–307

Van Noort R, Yarushina V (2018) Water, CO2 and argon permeabilities of intact and fractured shale cores under stress. Rock Mech Rock Eng 52(2):299–319. https://doi.org/10.1007/s00603-018-1609-8

Wang J, Tang D, Jing Y (2019) Analytical solution of gas flow in rough-walled microfracture at in situ conditions. Water Resour Res 55(7):6001–6017. https://doi.org/10.1029/2018wr024666

Wang C, Talandier J, Skoczylas F (2022) Swelling and fluid transport of re-sealed callovo-oxfordian claystone. Rock Mech Rock Eng 55(3):1143–1158. https://doi.org/10.1007/s00603-021-02708-4

Wanniarachchi WAM, Ranjith PG, Perera MSA, Rathnaweera TD, Zhang DC, Zhang C (2018) Investigation of effects of fracturing fluid on hydraulic fracturing and fracture permeability of reservoir rocks: an experimental study using water and foam fracturing. Eng Fract Mech 194:117–135. https://doi.org/10.1016/j.engfracmech.2018.03.009

Watanabe N, Hirano N, Tsuchiya N (2008) Determination of aperture structure and fluid flow in a rock fracture by high-resolution numerical modeling on the basis of a flow-through experiment under confining pressure. Water Resour Res 44(6):W06412. https://doi.org/10.1029/2006wr005411

Wenning QC, Madonna C, Kurotori T, Petrini C, Hwang J, Zappone A, Wiemer S, Giardini D, Pini R (2021) Chemo-mechanical coupling in fractured shale with water and hydrocarbon flow. Geophys

Res Lett 48(5):e2020GL091357. https://doi.org/10.1029/2020GL091357

Witherspoon PA, Wang JSY, Iwai K, Gale JE (1980) Validity of cubic law for fluid flow in a deformable rock fracture. Water Resour Res 16(6):1016–1024. https://doi.org/10.1029/WR016i006p01016

Yasuhara H (2004) Evolution of permeability in a natural fracture: significant role of pressure solution. J Geophys Res Solid Earth. https://doi.org/10.1029/2003jb002663

Yasuhara H, Elsworth D (2008) Compaction of a rock fracture moderated by competing roles of stress corrosion and pressure solution. Pure Appl Geophys 165(7):1289–1306. https://doi.org/10.1007/s00024-008-0356-2

Yasuhara H, Polak A, Mitani Y, Grader AS, Halleck PM, Elsworth D (2006) Evolution of fracture permeability through fluid–rock reaction under hydrothermal conditions. Earth Planet Sci Lett 244(1):186–200. https://doi.org/10.1016/j.epsl.2006.01.046

Yeo IW, De Freitas MH, Zimmerman RW (1998) Effect of shear displacement on the aperture and permeability of a rock fracture. Int J Rock Mech Min Sci 35(8):1051–1070. https://doi.org/10.1016/S0148-9062(98)00165-X

Zaouter T, Lasseux D, Prat M (2018) Gas slip flow in a fracture: local Reynolds equation and upscaled macroscopic model. J Fluid Mech 837:413–442. https://doi.org/10.1017/jfm.2017.868

Zhang C-L (2013) Sealing of fractures in claystone. J Rock Mech Geotech Eng 5(3):214–220. https://doi.org/10.1016/j.jrmge.2013.04.001

Zhang C-L, Talandier J (2022) Self-sealing of fractures in indurated claystones measured by water and gas flow. J Rock Mech Geotech Eng 15(1):227–238. https://doi.org/10.1016/j.jrmge.2022.01.014

Zhang Q, Fink R, Krooss B, Jalali M, Littke R (2021) Reduction of shale permeability by temperature-induced creep. SPE J 26(2):750–764. https://doi.org/10.2118/204467-Pa

Zhao YL, Zhang LY, Wang WJ, Tang JZ, Lin H, Wan W (2017) Transient pulse test and morphological analysis of single rock fractures. Int J Rock Mech Min Sci 91:139–154. https://doi.org/10.1016/j.ijrmms.2016.11.016

Zhou J, Zhang LQ, Li X, Pan ZJ (2019) Experimental and modeling study of the stress-dependent permeability of a single fracture in shale under high effective stress. Fuel 257:116078. https://doi.org/10.1016/j.fuel.2019.116078